Spin-Orbit Interaction and Landé g-factors in InAsSb Nanowires

Towards topological phase transitions

Author:
Joachim E. Sestoft

---

master's thesis

University of Copenhagen

Center for Quantum Devices

Academic advisors:

Ass. Prof. Peter Krogstrup

Post Doc. Mingtang Deng

Prof. Charles M. Marcus

Prof. Jesper Nygård

January 2017

Abstract

Topologically protected quantum computation based on braiding of Majorana zero modes is expected feasible in proximitized one-dimensional semiconductors. Theoretical proposals expect that the topological nature of Majorana zero modes could allow for quantum state manipulation by braiding, which is protected against decoherence. The material requirements for transitioning into the topological regime are: quasi one-dimensional nanowires with strong spin-orbit interaction, large Landé g-factors and induced superconductivity under parallel magnetic fields. This work presents measurements on spin-orbit interaction, Landé g-factors and induced superconductivity in $InAs_{1-x}Sb_x$ nanowires. Weak antilocalization measurements, on $InAs_{1-x}Sb_x$ nanowires with a step-like change in Sb concentration, x, along the nanowire axis, are fitted to extract the spin-orbit length as a function x. The spin-orbit lengths are converted into Rashba spin-orbit coefficients, where a maximum spin-orbit coefficient, $\alpha = 0.38$ meVÅ, is found for x $\sim$ 0.5. This finding is discussed in relation to recent theory proposing enhanced spin-orbit strength in $InAs_{1-x}Sb_x$ nanowires. Tunneling experiments on proximitized $InAs_{0.2}Sb_{0.8}$ nanowires show an induced hard superconducting gap of $\Delta = 230$ μeV and Landé g-factors of the order of $\sim$ 6-17. A topological phase transition is estimated to occur at a minimum magnetic field of B = 0.23 T, and indeed verified by measurements of Andreev bound states forming Majorana zero modes at B = 0.3 T and B = 0.38 T. This is the first report of Majorana zero modes in InAsSb nanowires. The same proximitized $InAs_{0.2}Sb_{0.8}$ nanowires are subjected to Coulomb charging experiments where $2e$ spaced Coulomb oscillations are evolved in a parallel magnetic field. A transition from a $2e$ to a $1e$ spacing as a function of magnetic field is observed; another signature of Majorana zero modes in InAsSb nanowires. From these findings it is discussed that ternary InAsSb nanowires could provide an alternate route to braiding of Majorana zero modes, where the spin-orbit coupling can be tuned by controlling the Sb/As ratio.

Acknowledgments

I want to thank Peter Krogstrup and Jesper Nygård for accepting me into your top-shelf research group. You have kept me on a long leash while still providing me with your supervision and guidance. This has only increased my interest in quantum transport and material science over the years. I want to thank Charles Marcus for accepting me into your *Majorana Team*. My increasing enthusiasm for quantum transport finally culminated when I was more or less permanently installed in front Triton 3 in the first half of 2016. I have learned a great deal from all the responsibility and possibilities you gave me. Your lessons on the art of discussing science and presenting intricate data I will not forget.

I want to extend my gratitude to Merlin von Soosten, who luckily sat next to me when I was first put in front of a dilution refrigerator in the fall of 2015. During our time at Triton 2, I could not have hoped for a better or kinder mentor - I hope I have adapted some of your hands-on mentality to science.

I want to extent my gratitude to Daniel Sherman for your introduction to Majorana physics and hours of discussing, whether it was science or politics. When on the topic of Majorana physics, Mingtang Deng cannot go unmentioned. I want to thank you for always having time to share your immense knowledge on this topic. Your calm and positive spirit is inspiring.

When I was transferred to "Team Weird-Materials" within the *Majorana Team*, it was decided that I should collaborate with Aske Gejl. Our long talks about life and science between lengthy 2D scans, are very precious to me. As a friend and colleague, I could not have asked for better. Sagde du CIV5...?

I want to extend my sincerest gratitude to Thomas Kanne, who has been a tremendous friend since day-one at the University of Copenhagen. I admire your positive spirit, your honesty, your hard-working mentality, your Jutlandish irony and your capability of staying 24 years old.

I want to thank Jakob Meyer-Holdt for teaching me all the clean-room basics

and the wonders of graphene. Our talks have been unique. Hopefully there are many more to come.

I want to thank my Canadian houseplant for being the best room-mate I could have hoped for. In the short time I've known you, you have really *grown* on me, and if you ever need a place to crash, you know which street I live on.

I want to thank Fuffi and Kringlen for all the fun we've had around the lab and in the night-life of Copenhagen. Hopefully there are many more to come.

I want to extent my deepest feelings of gratitude to my group of friends that are unrelated to my studies. I want to thank Theodor Thiele, Thobias Thiele, Peter Rohde, Anders Olesen, Andreas Henriksen, Daniel Ross and Sebastian Jezewski. Your ability to keep me grounded and letting it go unnoticed when I sometimes have been too tired to actively socialize, has been invaluable to me.

I want to thank my girlfriend Katrine Iversen, for being the person I've shared, and hope to keep sharing, all the everyday ups and downs with.

Last, I would like to extend my innermost gratitude to my father Hans, my mother Gunhild, and brother Jakob, for being the fantastic and peculiar family you are. It is hard to explain in words how much your unconditional help, understanding, strength and love, means to me. Tak for alt.

Joachim E. Sestoft
Copenhagen
January 2017

Contents

List of Figures

Motivation & Introduction 1

With *Intel* co-founder Gordon Moore's prediction in 1965, that the number of transistors that can be placed on an integrated circuit doubles roughly every two years, "Moore's Law" was born.[1] Sparked by the generally acknowledged ending of Moore's law, "The International Technology Roadmap for Semiconductors" (ITRS), a group of leading semiconductor industry experts decided to get to together and produce a road-map of the evolution of the semiconductor microchip as we know it today. Since the smallest commercially available microchips are around 10 nm, and the predicted size-limit by ITRS is 5 nm, the semiconductor industry is indeed approaching a cross-roads. Even *Intel*'s director of Component Research has admitted that things become foggy after the 7 nm limit.[2] On this scale the laws of quantum mechanics start to govern, e.g. a transistor with a size of 7 nm will experience quantum mechanical effects such as tunneling through its logic gates.[3] With the ever-growing demand for higher-performance computers and complex quantum mechanical simulations it seems the time is right to take the leap, and start using quantum mechanical laws to build the next generation computer.

In fact, it was already proposed by Richard Feynman in the 1980s[4] that the laws of quantum mechanics could be accessed in order make computer bits the size of atoms. This proposal was concretized by Di Vincenzo in 1997[5], where a list of

the minimum criteria for the quantum computer is sketched.

The criteria are:

- A distinct two-level system, a quantum bit (qubit), with a defined energy gap, must be readily a hand. This could entail two electronic spin states or the horizontal and vertical polarization of light.
- The ability to initialize the qubit into a simple fiducial state. This could be achieved by annealing a qubit into its ground state, in order to prepare the qubit for computation.
- A universal set of quantum gates. In classical computing algorithms that can be mapped onto bits are called gates. A series of these "universal" quantum gates are hence crucial for actual computation to be accessible.
- The ability to read-out the qubit before interactions with the environment causes the quantum state to decohere, i.e. the information is lost.

Turning our attention to the last criterion - naturally a question arises. How to read-out a quantum state before it decoheres? Similarly to error correction in classical computing, quantum error correction seeks to solve this issue. However, this requires almost error-free computation and is experimentally hard to implement. This exact issue is proposed to be bypassed by what is known as *topological quantum computation.*

Starting from the field of topology, which studies the properties of space that are protected under continuous deformation[6][i], we want to find a system which in the same manner is protected against continuous local perturbations.

Non-Abelian states of matter have been shown to possess this topological character.[8] We must consider the effects of interchanging particles in order to explain non-Abelian states. In three dimensions the exchange of two particles with an initial state Ψ will result in either a phase change of π producing the new state $-\Psi$, or the same initial state Ψ. These particles are called fermions and bosons. This property becomes very interesting if we go from 3 to 2 dimensions.

[i] Such deformations include stretching and bending, but not cutting or gluing.

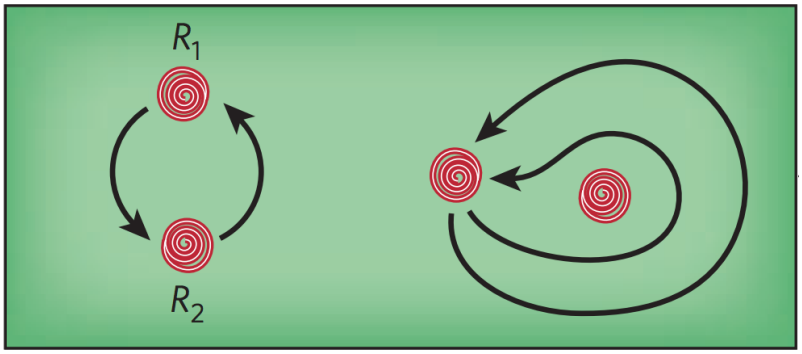

FIGURE 1.1: The ways of exchanging particles. **Left**) Particles R_1 and R_2 are exchanged. **Right**) Moving the particles around each other is equal to a double swap. Figure adopted from.[7]

The difference between 3 and 2 dimensional topology can be explained as such: Consider the image in fig. 1.1. In three dimensions a loop, such as the one seen on the right, can be continuously deformed so it does not loop the other particle anymore. This means that a double particle exchange will equal identity, and a single exchange can then only yield a phase of π or 0. On the other hand, restricting the loop to two dimensions a trivial loop cannot be made. Hence, a single exchange will produce a phase anywhere between 0 and π, which is also the reasoning behind the naming of this particle - "any"-ons. More interestingly, given certain criteria, exchange of these particles can lead to a different final state that is a unitary transformation of the initial system.[7] Or in other words, one can continually deform the particle Hamiltonian of two states into one another. This sort of braiding of particles is analogous to performing quantum state operations on the particles, and also the characteristic that qualifies them as non-Abelian anyons. The non-Abelian states are resilient to disturbances due to their topology while exchanging them allows one to perform quantum computational operations on them.[9] They are hence perfectly suited as a building-block for a quantum computer. Systems hosting non-Abelian anyons have been proposed[7], but their existance has not been definitively proven. A system that is proposed to host non-abelian anyons is the topological superconductor. Here, the non-Abelian anyons will take the form of Majorana fermions.

This thesis will focus on a solid state system that could host Majorana fermions, namely, semiconductor nanowires proximitized by a superconductor. The material requirements for a nanowire device to host Majorana fermions is summarized here, since they are the focus of the experimental section of this thesis. The requirements are[10]:

- Induced superconductivity.
- Large spin-orbit interaction.
- A large Landé g-factor.
- Quasi ballistic transport characteristics.

All but the last of the mentioned requirements will be investigated in a new system of ternary InAsSb nanowires. The main focus will be on how spin-orbit interaction and Landé g-factors can be used to transition proximitized InAsSb nanowires from the topological trivial phase, into the topologically protected.

Thesis Outline

The thesis is divided into 3 chapters.

1. The first chapter is concerned with the theory behind the material requirements required for the emergence of Majorana fermions. Starting with Kitaev's chain[9] it is shown that the Hamiltonian describing pairs of Majorana fermions in a p-wave superconductor can be mapped onto a Hamiltonian, which consists of s-wave superconductivity proximitized into a quasi one dimensional semiconductor nanowire with significant spin-orbit interaction, large Landé g-factors, in a magnetic field. Following are descriptions of the two Majorana spectroscopy methods that so far have produced indications of Majorana fermions in the solid state. Next, we dig deeper into the theory behind spin-orbit interaction in nanowires, and how to extract parameters such as spin-orbit length and spin-orbit phase coherence length. These details will be used later to discuss the experimental findings.

2. The second chapter is devoted to a short description of device fabrication and how a dilution refrigerator works. The chapter is terminated by a section on the generic measurement setup used in the later presented experiments.

3. The third chapter contains the findings from three distinct experiments. The first experiment is concerned with measuring the spin-orbit interaction in an $InAs_{1-x}Sb_x$ nanowire composed of segments of different Sb molar fractions. The second experiment involves tunneling experiments on $InAs_{0.2}Sb_{0.8}$ nanowires with Al grown on two facets. Here, proximitized superconductivity is demonstrated and the first observation of signatures of Majorana fermions in InAsSb nanowires is presented. These findings are discussed in relation to the spin-orbit interaction measurements of the first experiment. The last experiment involves Coulomb spectroscopy, also demonstrating signatures of Majorana fermions.

Theory 2

2.1 Experimental Majorana Fermion Crash-Course

This section seeks to explain the theory behind Majorana fermions in condensed matter systems from an experimentalists perspective. It will be presented with a special focus on how to create Majorana fermions in semiconductor nanowires. This section will be based mostly on the publication by Leijnse et al. called *Introduction to topological superconductivity and Majorana fermions.*[11].

Majorana fermions were first hypothesized by Ettore Majorana in 1937 as real solutions to the Dirac equation.[12] They differ in their characteristic from Dirac fermions in that they are their own antiparticle, or more rigidly speaking, $\Psi = \Psi^\dagger$, where Ψ is the annihilation operator and $\Psi^\dagger$ is the creation operator. This characteristic stems from Majorana's initial suggestion that spin-1/2 particles can be expressed as real wave equations, and are hence related by complex conjugation, such that they are their own antiparticle.

The sum of two Majorana fermions, can be rewritten into an ordinary fermion,

$$f = \frac{\gamma_1 + i\gamma_2}{2}$$

where f is the annihilation operator, and γ_i is the Majorana fermion operator.

Expressing the Majorana fermion operators in terms of fermionic operators, yields the inverse relationship,

$$\gamma_1 = f + f^\dagger$$

$$\gamma_2 = i(f - f^\dagger)$$

which proves the that Majorana fermions are their own antiparticle $\gamma = \gamma^\dagger$. Experimentally speaking, this statement has little sense if the Majorana fermions are not spatially separated, and can be addressed separately.

Occupation of Majorana modes and fermionic states cannot be compared, as seen using the fermionic anti-commutation relation $\{\gamma_i, \gamma_j\} = 2\delta_{ij}$, which yields that $\gamma_i^\dagger \gamma_i = \gamma_i^2 = 1$. Instead one can describe the Majorana fermions by their fermionic state operator $|n_1, n_2, ...n_N\rangle$, where $n_i = f_i^\dagger f_i$. By spatial separation of the Majorana fermions, there is no interaction, and their energy is zero. This is achieved independent of whether the corresponding fermionic state is occupied or not - hence, all Majorana fermions are in a degenerate ground state. Consider the sum of the fermionic occupation, $\sum_{i=1}^{N} n_i$, the state can be either even or odd. This also describes the parity of the state. This will be described more thoroughly in the next section where it is found out that the odd charge state corresponds to two Majorana fermions.

It can be shown that exactly four of these ground states can be defined into a two-level system - or a topological qubit. The two-level system consists of two fermionic states with the same parity that describe the qubit states 0 and 1 by the even fermionic number state, $\{|00\rangle, |11\rangle\}$, and the odd $\{|01\rangle, |10\rangle\}$. It is shown that braiding of the ground states around each other has the capacity to bring the fermionic number state from one ground state to another. Importantly, this way of braiding states into each other is order dependent, which is a criteria that has to be fulfilled in order for the Majorana fermions to obey non-Abelian exchange statistics.

So far, braiding operations alone do not cover all necessary operations that are needed to compute quantum algorithms. Recall that this is one of the criteria

proposed by DiVincenzo: a universal set of quantum gates. However, a full set can be accomplished by adding a set of operations that are not topologically protected.

Hence, constructing Majorana fermions in the solid state offers two great incentives: (1) the possibility of detection of non-Abelian states of matter and (2) that these may allow for fault tolerant quantum computation.

2.1.1 Kitaev Chain

This section is devoted to describing the Kitaev chain [9] - or colloquially speaking Kitaev's toy model. Kitaev's toy model describes how Majorana fermions are created in spin-less p-wave superconductors.

The Kitaev chain Hamiltonian describes a 1-dimensional spin-less p-wave superconductor in which eigenstates would be spatially separated Majorana fermions. Starting with the 1-dimensional tight-binding chain with p-wave superconducting pairing,

$$H_{chain} = -\mu \sum_{i=1}^{N} n_i - \sum_{i=1}^{N-1} (t c_1^\dagger c_{i+1} + \Delta c_i c_{i+1} + h.c.) \tag{2.1}$$

where, μ is the chemical potential, $h.c.$ is the hermitian conjugate, c_1 is the electron annihilation operator at the site i, $c_1^\dagger$ is the electron creation operator at the site i , $n_i = c_1^\dagger c_i$ denotes the number operator, Δ is the superconducting gap and t is the hopping amplitude. The equation does not entail spin indices since we only consider one spin, i.e. it is a spinless system. No site can be doubly occupied due to Pauli's exclusion principle, and pairing occurs between electrons with equal spin. See fig. 2.1 **a** for a schematic of Kitaev's toy model.

Splitting the fermion into its real and imaginary parts reveals that fermion can be described by two Majorana fermions,

$$c_1 = \frac{1}{2}(\gamma_{i,1} + i\gamma_{i,2}) \tag{2.2}$$

$$c_2^\dagger = \frac{1}{2}(\gamma_{i,1} - i\gamma_{i,2}), \tag{2.3}$$

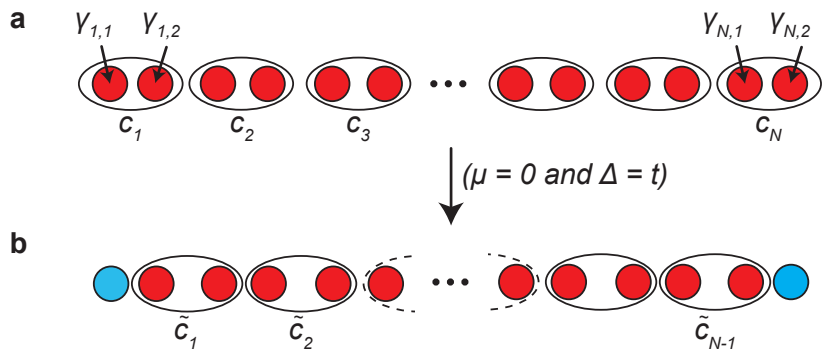

Figure 2.1: One-dimensional tight-binding model of a 1-dimensional a p-wave superconductor. **a)** At each position i, the fermionic operators (in this case only the annihilation operator c is shown) is composed of two Majorana operators, $\gamma_{i,1}$ and $\gamma_{i,2}$. **b)** When μ is zero and Δ are equal to the hopping amplitude, t, the fermionic operators consist now of a new set of Majorana operators, namely $\gamma_{i+1,1}$ and $\gamma_{i,2}$. At Δ and μ equal to zero, the two Majorana operators $\gamma_{1,1}$ and $\gamma_{N,2}$ are left unpaired (the blue balls). These unpaired Majorana operators can be combined into a zero energy non-local fermion operator $\tilde{c}_M$.

where $c^{(\dagger)}$ is the annihilation (creation) operator and γ is the Majorana operator[i].

At the given limit $\mu = 0$ and $t = \Delta$ and inserting eq. 2.2 and 2.3 into 2.1 yields

$$H_{chain} = -it \sum_{i-1}^{N-1} \gamma_{i,2}\gamma_{i+1,1}, \tag{2.4}$$

which turns out to be a different way of writing the diagonalized Hamiltonian. Eq. 2.4 now expresses the new coupling of Majoranas composed of neighboring fermions - this can be written as

$$\tilde{c}_i = \frac{\gamma_{i+1,1} + i\gamma_{i,2}}{2}. \tag{2.5}$$

Rewriting the Hamiltonian in terms of the newly found fermionic operators yields,

[i]If these equations are inverted they yield $\gamma_{i,1} = c_i^\dagger + c_i$ and $\gamma_{i,2} = ic_i^\dagger - c_i$. It is evident that the γ's are indeed Majorana operators because they are hermitian.

$$H_{chain} = 2t \sum_{i=1}^{N-1} \tilde{c}_i^\dagger \tilde{c}_i, \tag{2.6}$$

and reveals an energy of these states that is equal to 2t. A sketch of this situation is seen in fig. 2.1 **b**. An important note here is that the Majorana pair at the ends of the chain are missing from eq. 2.4. The Majorana states at the extremity of the chain can be expressed as,

$$\tilde{c}_M = \frac{1}{2}(\gamma_{N,2} + i\gamma_{1,1}), \tag{2.7}$$

where $\tilde{c}_M$ is a single fermionic operator. This state is indeed non-local since it is composed of two Majorana operators that are spatially separated to the two ends of the chain. Additionally, since this operator is not included in the Hamiltonian it is proof of its zero energy occurrence. The state will always have zero energy whether it is occupied by a fermion ($\tilde{n}_M = \tilde{c}_M^\dagger \tilde{c}_M = 1$) or empty ($\tilde{n}_M = \tilde{c}_M^\dagger \tilde{c}_M = 0$), which means that it is a two-fold degenerate state. Kitaev et al. show that these non-local end states do not only exist at $\Delta = t$ and $\mu = 0$, but can occur also if the chemical potential lies within the gap $|\mu| < 2t$. Experimentally speaking the states are not strictly localized at the ends but have an exponentially decaying expectation value from the ends, hence the Majorana fermions are only zero energy if they are separated for the wave-functions not to overlap.

The occurance of Majorana fermions in one-dimensional nanowires can be described by,

$$H_{1D}^{pw} = \int dx \left[\Psi^\dagger(x) \left(\frac{p_x^2}{2m_e^*} - \mu \right) \Psi(x) + \Psi(x)|\Delta| p_x \Psi(x) + h.c. \right],$$

where m_e^* is the effective electron mass, p is the momentum and $\Psi^{(\dagger)}$ is the real-space annihilation (creation) operator. The phase term is omitted. However, experimental realization of this model requires p-wave pairing which is proposed to exist in materials not readily at hand. Luckily, there are ways around this.

2.1.2 Majorana fermions in hybrid semiconductor-superconductor nanowires

Yuval Oreg and Roman Lutchyn proposed in 2010 a simpler and "less exotic" version of Kitaev's Hamiltonian[10], with all the tools readily at hand in condensed matter labs. Consider the sketch in fig. 2.2 where the proximitized nanowire is positioned with a proximity strength Δ parallel to the y-axis, the spin-orbit interaction, u, along the z-axis and the magnetic field along the x-axis. The Hamiltonian of this system is given as,

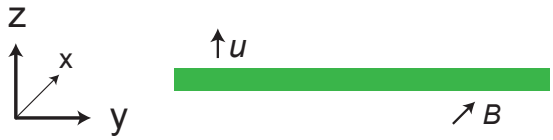

Figure 2.2: Proximitized nanowire positioned accordingly to the orientation of relevant fields. The proximitized nanowire is positioned parallel to the y-axis, the spin-orbit interaction along the z-axis and the magnetic field along the x-axis.

$$H = [p^2/2m^* - \mu(y)]\tau_z + \alpha k_x \sigma_z \tau_z + B(y)\sigma_x + \Delta(y)\tau_x, \tag{2.8}$$

where μ is the chemical potential, σ and τ is the Pauli matrices operating in spin space and particle-hole space, respectively. k_x is the momentum vector. For the moment consider the Zeeman energy, the superconducting proximity effect and the spin-orbit interaction omitted. The first part of eq. 2.8 is the kinetic energy term whose dispersion relation is a parabola, as seen in fig. 2.3 **a**. Introducing spin-orbit interaction the conduction band is shifted left and right in momentum space by $k_{SO} = \mathrm{m}\alpha$ and down by spin-orbit energy by $\mathrm{E}_{SO} = \frac{m \cdot \alpha^2}{2m}$ as seen in fig. 2.3 **b**. α is the Rashba spin-orbit coefficient and m is the effective mass. The spin-degeneracy is still intact since time-reversal symmetry is not broken.

An externally applied magnetic field will break the time-reversal symmetry and opens a gap at k = 0, as seen in fig. 2.3 **c**. The gap size is determined by the Zeeman energy, $\mathrm{E}_Z = g\mu_B B$, where μ_B is the Bohr magneton, B is the external

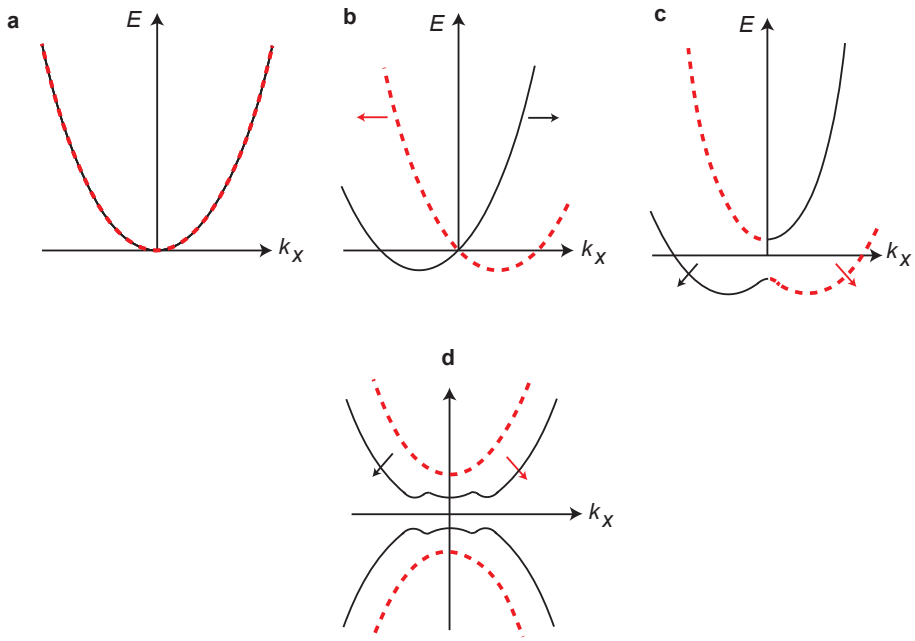

FIGURE 2.3: The progression of the dispersion relation of a proximitized and spin-orbit coupled nanowire in a magnetic field. The evolution is depicted in a series of graphs from **a**) to **d**). **a**) The degenerate dispersion relation described by the first part of the Hamiltonian, $p^2/2m^* - \mu(y)$, depicted as a parabola. **b**) The spin-orbit interaction splits the dispersion into two spin-polarized bands. Additionally the bands are moved down in energy by the spin-orbit interaction $E_{SO} = \frac{m \cdot \alpha^2}{2m}$. **c**) The magnetic field which is orthogonal to the spin-orbit field opens a gap at the crossing of the bands of the size of the Zeeman energy, E_z. **d**) The proximitized superconductivity is turned on and the topological gap opens between the electron and hole band.

magnetic field and, g, is the Landé g-factor. The states residing within the gap created by the Zeeman energy are now effectively spin-less, i.e only one type of spins exist in the gap. If μ is placed within the gap spin-less carriers are induced. The superconductivity pairing term Δ gives rise to a gap in the dispersion relation where electron and hole bands are separated. This effect arises due to Cooper pair condensation of electron within $\pm\Delta$ around the Fermi energy. For a small Δ the effective superconducting gap is deemed topological because of the external magnetic field. This effect is associated with Majorana zero modes, which are condensed matter analogues to Majorana fermions discussed earlier. It is still

undetermined whether or not Majorana zero modes indeed are Majorana fermions, until these have been braided and their non-Abelian nature have been proven. From now on the term Majorana zero mode will be used.

At the exact point where the gap as seen in fig. 2.3 **d** closes, the transition from the topologically trivial phase into the topological superconducting phase occurs. At this point the Majorana zero modes appear. This gap can be described as $E_0 = |B - \sqrt{\Delta^2 + \mu^2}|$. In the case for $B^2 > \Delta^2 + \mu^2$ there is a strong interaction induced gap, i.e. the nanowires is in its topological phase. For $B^2 < \Delta^2 + \mu^2$ the nanowires is pairing dominated, i.e no ends states. At exactly $B^2 = \Delta^2 + \mu^2$, the phase transition occurs.

2.2 Majorana Spectroscopy

This section explains two ways of detecting Majorana zero modes realized in 1-dimensional nanowires. Beginning with the first reported Majorana signature from the Technical University in Delft in 2012.[13] This geometry is called *Delft*. The second geometry is also dubbed by its city of origin, namely the *Copenhagen* device which showed its first Majorana zero mode in 2016.[14]

2.2.1 The *Delft* Geometry

The *Delft* geometry is a tunnel probe consisting of a normal metal, (N), an insulator, (I), and a superconductor on top of the nanowire inducing superconductivity, (S). As seen in fig. 2.4 **a** the nanowires is colored green, (NW), the superconductor colored blue, (SC), and the normal metal leads, (Ti/Au), colored yellow. This constitutes the NIS device as seen in fig. 2.4 **b**.

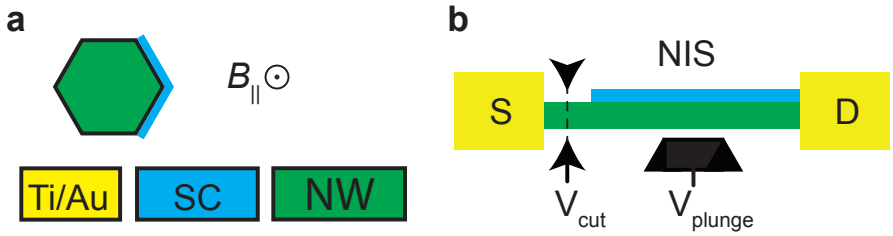

FIGURE 2.4: The schematics for the *Delft* tunneling device. **a**) Nanowire cross-section with according coloring scheme. Normal metal leads are colored yellow, the superconductor colored blue and the nanowire colored green. The parallel orientation of the magnetic field, $B_{\parallel}$, according to the nanowire axis is indicated. **b**) The layout of the device starting from left: Normal metal lead connected (N) to a bare nanowire section. In close proximity to the bare nanowire section the V_{cut} gate is used to create the tunneling barrier (I). A strip of superconductor has either been deposited or grown onto the nanowire which is contacted by another normal metal lead (S). These three components constitute the NIS device. The V_{plunge} gate is in close proximity to the superconducting part of the nanowire tuning the number of modes.

By tuning of the gate denoted V_{cut} the bare semiconductor nanowire part is used to create a potential barrier, effectively making it I and tuning the device into the tunneling regime where $dI/dV \ll g_0 = 2e^2/h$. dI/dV is differential

conductance and g_0 is the quantum of conductance. Tunneling of charge carriers at $E < \Delta$ into the superconducting segment will only occur through the process of Andreev reflection.[15] Consider an electron of energy $\mu + E < \Delta$ traveling from the normal metal incident to the superconductor, no states are free to enter. However, through the process of retro-reflection of a hole with the same momentum at energy $\mu - E < \Delta$, a Cooper pair of charge $2e$ can be transferred into the superconductor at the Fermi energy. If a bias voltage is applied across the interface the system changes dramatically. If an electron is moving incident to the barrier and gains energy eV the hole traveling the opposite way also gains E = eV. Thus, by multiple Andreev reflections, bound states in the interface can gain arbitrarily high energies - also called Andreev bound states (ABS).[16]

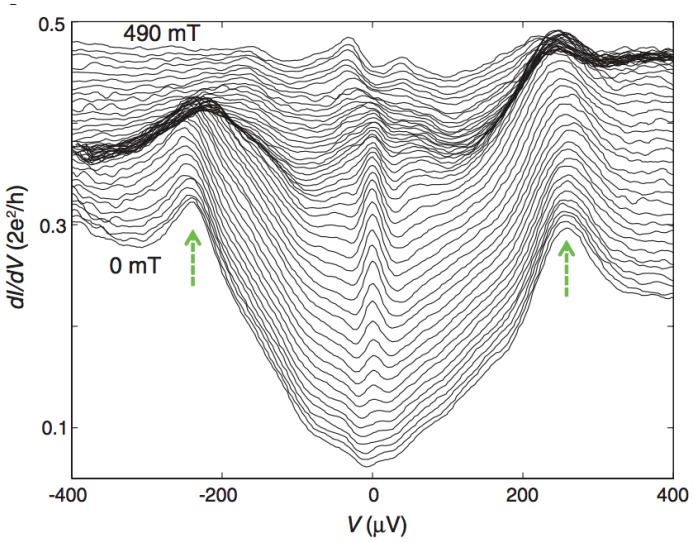

Figure 2.5: The Majorana zero modes signature found in a tunneling experiment by Mourik et al.[13] in Delft, the Netherlands. Conductance, dI/dV, as a function of source drain bias, V, and magnetic field, $B_{\parallel}$. Traces are offset for clarity. The green arrows indicate the superconducting coherence peaks from which ABS move away and merge at E = 0. The displacement of the ABS is hidden in the relatively high sup-gap conductance, as discussed by Mourik et al.

Without spin-orbit interaction and magnetic field, the ABS have a uniform weight along the axis of the nanowire. This is analogous of quantized modes in the nanowire. Turning on spin-orbit interaction these states are localized in the

ends of the nanowire. When the magnetic field is turned on the spin degeneracy is lifted and the states are split. With increasing magnetic field these states move closer to E = 0 until they merge and form a Majorana zero mode at E = 0.[17]

Exactly this is achieved in InSb nanowires proximitized by NbTiNi as seen in the waterfall plot in fig. 2.5, adopted from[13]. Here, differential conductance is shown as a function of source-drain bias, V, and parallel magnetic field, $B_{\parallel}$. The two green arrows show the superconducting coherence peaks indicating the superconducting gap with $\Delta = 220\ \mu$eV. At $B_{\parallel} = 100$ mT the characteristic zero bias peak emerges, as unresolved ABS states merge. Likely, these are hidden in the relatively large sub-gap conductance.

2.2.2 The *Copenhagen* Geometry

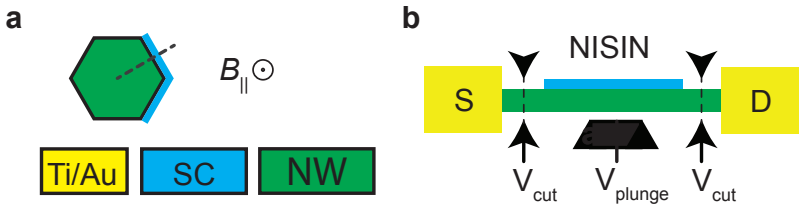

FIGURE 2.6: The schematics for the *Copenhagen* Coulomb charging device. **a**) Nanowire cross-section with according coloring scheme. Normal metal leads are colored yellow, the superconductor colored blue and the nanowire colored green. The parallel orientation of the magnetic field $B_{\parallel}$ is indicated with relation to the nanowire axis. The two normal metal leads (N) are tuned into a tunnel coupling regime by the two V_{cut} gates (I). Isolated from the normal metal leads a superconducting shell is proximitizing the nanowire (S). Effectively this becomes an NISIN device which can be thought of as a superconducting quantum dot. The occupation of the quantum dot is tuned by V_{plunge}.

The *Copenhagen* geometry is a charge probe experiment, composed of an isolated nanowire island with proximitized superconductivity. As seen in fig. 2.6 **a** the same colouring scheme as for the *Delft* device is used here. The geometry constitutes a normal metal-insulator-superconductor-insulator-normal metal (NISIN) layout, as seen in fig. 2.6 **b**.

The tunnel coupling of the superconducting island to the normal metal leads is

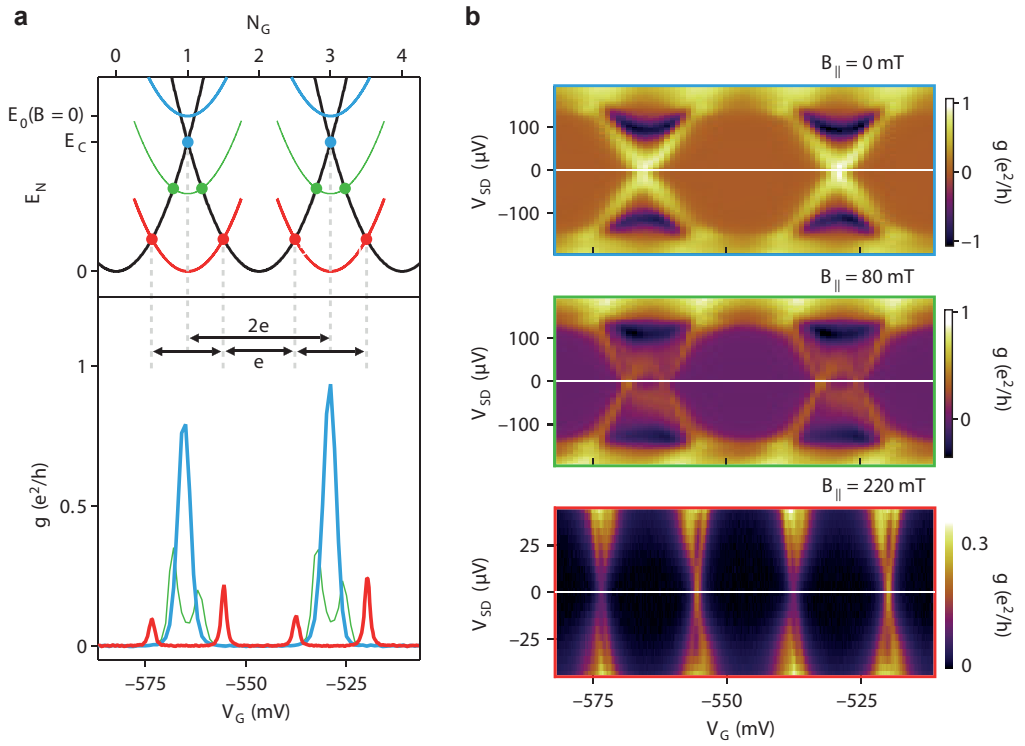

Figure 2.7: The Majorana zero mode signature found in a Coulomb charging experiment performed by Albrecht et al.[14] in Copenhagen, Denmark. **a**) Top: The even (odd) ground state energies are black (coloured). Transport can only occur where the parabolas intersect. In regimes with even occupation (N) the light blue band is shown. Even and odd charge states are coloured green. For the E_0 = 0 case (or the Majorana zero mode case) the trace is coloured red. Bottom: Differential conductance, g, as a function of gate voltage, V_G, shows traces at different magnetic fields at source drain voltage V_{SD} = 0. The red trace is an evenly spaced 1e Coulomb oscillation spacing characteristic of a zero energy state. **b**) Conductance as a function of V_{SD} and V_G in a parallel magnetic field of magnitudes B = 0, 80 and 220 mT. Top: Evenly 2e spaced Coulomb diamonds. Middle: The odd charge state becomes favorable as a function of $B_{\|}$. Bottom: Fully transformed 1e spaced Coulomb diamonds.

established by tuning the two cutter gates, V_{cut}, essentially creating a superconducting quantum dot tunnel-coupled to two normal metal leads. Within the induced superconducting gap, Δ, only tunneling of Cooper pairs of charge 2e is permitted. By sweeping of V_{plunge} the charge states on the superconducting island can be brought on/off resonance with the leads, as similarly observed in superconducting

metallic islands[18]. Here, the formation of evenly spaced $2e$ Coulomb diamonds within Δ are observed. Applying a parallel magnetic field will change the distance between the Coulomb resonances from $2e$ to $1e$. This characteristic is proposed as a signature of Majorana zero modes.[19;20]

The transition from $2e$ to $1e$ is shown in proximitized InAs nanowires in a parallel magnetic field.[14] As seen in fig. 2.7 **a** increasing the parallel magnetic field $B_{\parallel}$ the Zeeman energy lowers the energetically unfavorable odd charge state to E = 0 (figure adopted from[14]). The measurement characteristic phenomenon is shown in the bottom of fig. 2.7 **a**, where two equidistant Coulomb oscillations transition into four equidistant Coulomb oscillations. The evenly $2e$ spaced Coulomb diamonds, as seen in fig. 2.7 **b**, are evolved in a parallel magnetic field where a doubling in number of Coulomb diamonds at $B_{\parallel}$ = 220 mT has occurred.

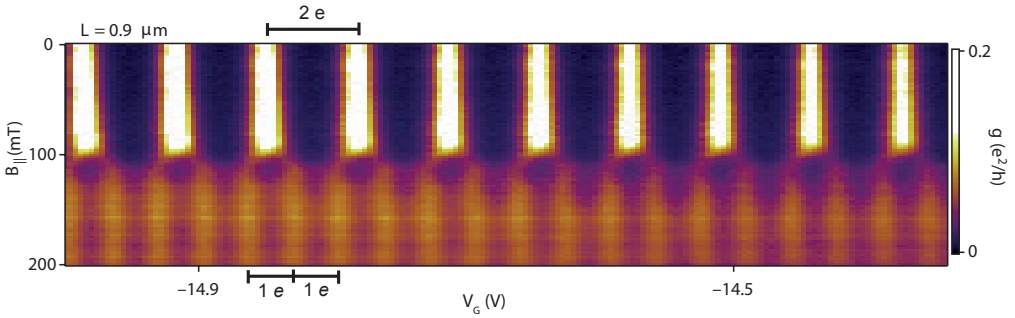

FIGURE 2.8: Another Majorana zero mode signature found in a Coulomb charging experiment performed by Albrecht et al.[14] in Copenhagen, Denmark. Differential conductance, g, as a function of V_G and parallel magnetic field performed at a source drain bias of $V_{SD} = 0$. Here, a series of $2e$ spaced Coulomb peaks at $B_{\parallel} < 100$ mT are shown, that evolve into nearly $1e$ spaced Coulomb peaks at $B_{\parallel} > 100$ mT. The intensity dimming at the beginning of the splitting is evident of Majorana fermion teleportation.

This evolution is, additionally, verified in fig. 2.8 where differential conductance, g as a function of V_G and parallel magnetic field is shown. The Coulomb oscillations measured at a source drain bias of $V_{SD} = 0$ start splitting at $B_{\parallel} \sim 100$ mT and a transition from a $2e$ to a $1e$ periodicity is confirmed at $B_{\parallel}$ = 125 mT. The intensity is reduced when the splitting initiates and regains strength when the splitting has finished, consistent with what is theoretically proposed as Majorana

teleportation.[21]

2.3 Spin-Orbit Coupling in 1-dimensional semiconductor nanowires

We now change our focus onto a more detailed discussion of the spin-orbit coupling in nanowires. We will start from quantum diffusive transport, move into universal conductance fluctuations, discuss time-reversed paths and briefly explain magneto-conductance. At last, these topics will be combined into a quantitative expression for weak antilocalization effects in nanowires.

2.3.1 Quantum Diffusive Transport

At very low temperatures the wave nature of electrons influence the conductance via quantum interference. Typically quantum interference phenomena are studied by measuring conductance when a magnetic field or electrostatic potential is swept. [22]

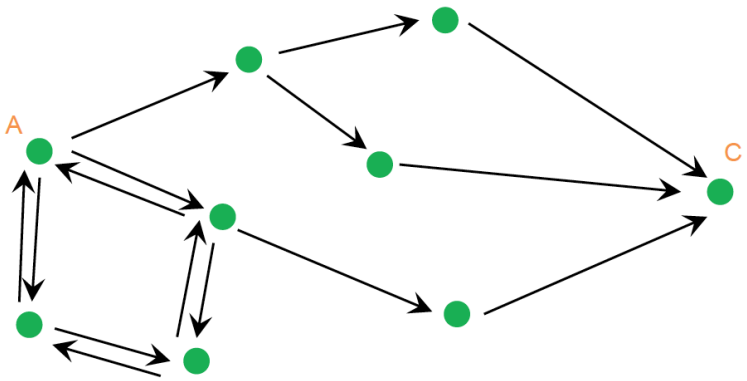

FIGURE 2.9: Wave paths producing quantum interference in a diffusive system. Electron waves split into partial waves traverse from **A** to **C** via different paths. The different paths are illustrated with arrows. Counter- and clockwise propagation in a loop leads to electron interference. Figure adopted from. [23]

Consider the schematic in fig. 2.9 and assume that phase coherence length, the length at which the phase is randomized, l_ϕ, is longer than the distance from **A** to **C**. In this case electrons act as waves and can thus split up into partial waves

traversing numerous diffusive paths from **A** to **C**. We can describe each partial wave by a complex amplitude C_j,

$$C_j = c_j e^{i\phi_j} \tag{2.9}$$

where ϕ_j is the phase the partial electron wave has gained by traveling from **A** to **C** by a path j. If one squares the sum over all the partial wave amplitude contributions, the propagation probability from **A** to **C** is

$$P_{AC} = |\sum_j c_j e^{i\phi_j}|^2 = \sum |c_j|^2 + \sum_{l,k\neq l} c_l c_k cos(\phi_l - \phi_k). \tag{2.10}$$

where the correction to the classical term ($P_{AC}^{cl} = \sum_j |c_j|^2$) is expressed in the second term. A change in gate voltage will affect the interference contribution to P_{AC} , because the phase added along the path is $\phi \sim \int \vec{k} \cdot d\vec{l}$, where $\vec{k}$ is the wave vector and $d\vec{l}$ is the propagation direction. The electron density will change when a electrostatic gate potential is changed, hence $\vec{k}$ changes and results in a change in P_{AC}. The random distribution of ϕ will average out if a large number of paths, j, exist, making $P_{AC} = P_{AC}^{classical}$.

2.3.2 Universal Conductance Fluctuations

The transmission between two contacts gives the conductance of a sample. As described above the square of the sum of the complex valued transmission amplitudes lets one obtain the transmission probability.[22] Similar to the interference described above Universal Conductance Fluctuations (UCF) can be understood by considering a number of paths, γ_i, for simplicity consider only two, namely, γ_1 and γ_2. The two wave paths contributing to transmission from contact 1 to contact 2 are illustrated in fig. 2.10. Pairs of paths can have the same start and ending point and thus span an area between them. Conductance fluctuations could be described based on Aharonov-Bohm oscillations in a small magnetic field, however, here the B = 0 case will be considered.

Phase differences that would cause averaging effects due to statistical distributions of enclosed areas are not occurring because of the microscopic nature of the

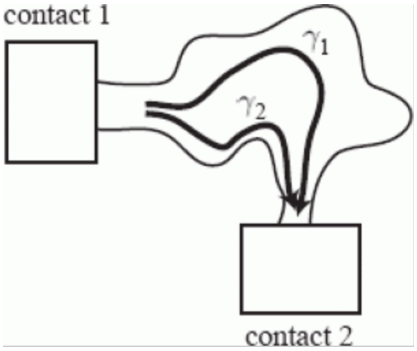

FIGURE 2.10: A mesoscopic sample composed of two contacts and a number of paths γ in between. Two paths, γ_1 and γ_2, are seen, that contribute to the total transmission through the sample. Figure adopted from [22].

sample, e.g. a nanowire. Hence, conductance fluctuations observed as a function of electron density can be observed because the phase of each path is modified by the change in Fermi velocity. This means that γ_1 and γ_2 will interfere constructively and destructively as a function of a gate voltage. These fluctuations are stable and reproducible in time. In diffusive systems where the electron paths are highly dependent on elastic scattering this effect is known as *universal conductance fluctuations* because it is theoretically proposed that for $T \to 0$ the amplitude of the conductance fluctuations will be on the order of e^2/h. This effect should only be evident if l_ϕ is on the order of the sample size [22].

2.3.3 Time-reversed paths

When the electron waves traverse in a circular motion and reach the same origin ($\mathbf{A} = \mathbf{C}$), no averaging effects due a large number of paths, j, occur. The waves propagating along the same path clockwise and counter clockwise will constructively interfere since the added phase along the path will be the same. This way the complex amplitude is the same for both paths, $c_1 = c_2$, and conversely twice the amplitude is obtained [22]

$$P_{AA} = c_1^2 + c_2^2 + 2c_1c_2 = 4c_i^2 = 2P_{AA}^{cl}. \tag{2.11}$$

This way, constructive interference of electron waves in a closed path increase the probability of the electron to end up at its initial position and increasing resistance. This effect is valid for all closed loops as long as l_ϕ is larger than the circumference of the loops and will thus not be averaged out.

From Einstein's relation,

$$\sigma = e^2 N(0) D, \tag{2.12}$$

where σ is conductance, e is the electron charge, N(0) is the density of states at the Fermi level and D is the diffusion constant, a quantitative approach can be found.[24] Assuming that classical transport yields $D = \frac{1}{n} v_F l_e$, where l_e is the electron mean free path, v_F is the fermi velocity and n is the number of dimensions. Electrons are assumed to follow classical paths which requires that the Fermi wavelength, λ_F is smaller than l_e. The Fermi velocity and mean free path is related via the scattering time, τ_e, via $l_e = v_F \tau_e$. The diffusion constant is modified by quantum interference producing ΔD, which in turn gives a correction to the conductance, $\Delta\sigma$. ΔD stems from a consideration of the direction of electron waves in the quantum coherent return paths, the effective area and the chance to end up in the same area through diffusive motion. These considerations give in combination with equation 2.12 rise to,

$$\Delta\sigma = -\frac{2e^2}{\pi\hbar} D \int dt C(t) e^{-\frac{t}{\tau\phi}} \left(1 - e^{-\frac{t}{\tau_e}}\right). \tag{2.13}$$

Here, $C(t)\left[\frac{1}{m^3}\right]$ is the classical probability of return, and is described by the diffusion equation. This way of describing electron motion as a classical diffusive motion is only valid for time scales much longer than the time between collision, τ_e.

2.3.4 Magnetoconductance

Magnetic fields will alter electron interference[25]. Again, consider Fig. 2.9 where the path from **A** to **C** adds an extra phase difference,

$$\phi(t) = \frac{e}{\hbar}\int_A^C \vec{A}\cdot d\vec{l}$$

when a magnetic field is applied B, where $B = \nabla \times A$. ∇ is the vector differential operator and A is the vector potential. When the different closed paths explained in fig. 2.9 are subjected to a magnetic field they will experience a phase shift,

$$\phi(t) = \pm 2\pi \frac{\Phi}{\Phi_0},$$

where $\Phi_0 = \frac{h}{e}$ is the magnetic flux quantum , Φ is the flux, and the plus/minus sign referring to whether the electron is travelling clockwise or counterclockwise. Between the clockwise and counterclockwise paths the phase difference is then $4\pi\frac{\Phi}{\Phi_0}$, hence the constructive interference is canceled. If there is a large number of closed paths with distinct areas the magnetic field will average out the interference term in equation 2.11. This way the conductance suppression is only seen for small magnetic field magnitudes and will disappear at larger magnetic field retrieving the classical conductance. This way a positive magnetoconductance is observed for a zero magnetic field.

2.3.5 Spin-orbit interaction

This section concerns how spin-orbit interaction interacts with quantum interference. Spin-changes along closed paths can occur due to scattering.[22] Consider the inital spin state $|s\rangle = (a, b)^T$, where T is the transpose. After a clockwise rotation,

$$|s'\rangle = R|s\rangle,$$

where R is the rotation. A number of small rotations R_i occurring during, or in between scattering events, describes the change in spin, and if the product of all rotational changes is taken into account $R = R_N ... R_2, R_1$, is obtained. On the other hand the spin state along a time-reversed path will experience a spin change that is occurring in the opposite order, hence each angle of rotation is inverted, such that the last spin state is $|s''\rangle = \tilde{R}|s\rangle$. Here, the $\tilde{R}$ is composed of $\tilde{R} = \tilde{R}_N ... \tilde{R}_2, \tilde{R}_1$, with $\tilde{R}_i = R_i^{-1}$.

The effect of spin-orbit interaction on quantum interference is best seen when the interference term of eq. 2.11 is multiplied with $2\langle s'|s''\rangle = 2\langle s|R^2|s\rangle$. If the spin-orbit interaction is weak the trajectories along the time-reversed paths will not experience much spin rotation. Hence, the correction to the quantum interference term can be approximated to $R^2 \sim 1$, i.e. spin-orbit interaction does not modify the quantum interference. However, R^2 must be calculated for stronger spin-orbit interaction. Consider the 2×2 matrix, R, for spin-$\frac{1}{2}$ rotation over the three arbitrary angles α, β and γ. Averaging this over a large number of diffusive paths one obtains $\langle s|R^2|s\rangle = -\frac{1}{2}$.[22] The return probability P_{AA} in eq. 2.9 is then reduced by the spin-orbit interaction. The small increase in conductance is dubbed weak anti-localization (WAL). In other words, the localization effect arising from quantum interference is *weakly* canceled, or at higher magnetic fields changed back to classical conductance. It is here assumed that the magnetic field only interacts with spin, not accounting for the Zeeman effect.

2.3.6 Spin-orbit interaction and magnetoconductance nanowires

This section combines the expressions found for the quantum interference, spin-orbit interaction and magnetic field dependence in the previous sections. The combined expression is a correction to the classical conductance in a nanowire and its interaction with a magnetic field[23],

$$\Delta G(B) = -\frac{2e^2}{h}\frac{D}{L}\int_0^\infty dt C(t)\left(1 - e^{\frac{-t}{\tau_e}}\right)e^{\frac{-t}{\tau_\phi}}e^{\frac{-t}{\tau_B}}\frac{1}{2}\left(3e^{\frac{-4t}{3\tau_{SO}}} - 1\right), \qquad (2.14)$$

where $\Delta G(B)$ is the conductance modification as a function of magnetic field. Additionally, it is assumed that the magnetic field dephasing has an exponentially decaying average phase factor, $e^{-\frac{t}{\tau_B}}$, with the characteristic time τ_B, due to geometry confinement. L is the length of the device.

In order to investigate how eq. 2.14 applies to a nanowire with a width, W, coherent backscattering due to confinement[26] which occurs when the $l_\phi > W$, is evaluated. Additionally it is required that $\lambda_F \ll W$, or in other words that a lot of subbands (or modes) contribute to transport, in order for the semi-classical approach to be valid. These requirements force the nanowire to act as

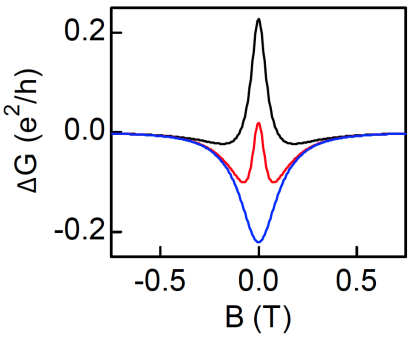

FIGURE 2.11: Black trace shows WAL without localization at larger magnetic fields when B when $l_{SO} \sim l_e$. Parameters are $l_{SO} \sim 200$ nm and $l_\phi \sim 800$ nm . Red trace shows $l_{SO} \sim 400$ nm and $l_\phi \sim 800$ nm. Blue shows $l_{SO} \sim 800$ nm and $l_\phi \sim 400$ nm. Figure adopted from [23].

one-dimensional in terms of phase coherence length, but still with a large number of modes contributing to transport. Diffusion back to the initial point of departure in a one-dimensional system is given as $C(t) = \frac{1}{\sqrt{4\pi D t}} \frac{1}{W^2}$, with $D = \frac{1}{3} v_F l_e$. In other words, the dimensional confinement in a nanowire contributes to the chance of back-scattering more than if one considers two or three-dimensional systems. By insertion of these modifications eq. 2.14 assumes the form,

$$\begin{aligned}\Delta G = -\frac{2e^2}{hL}\Bigg(&\frac{3}{2}\left[\frac{1}{l_\phi^2}+\frac{4}{3l_{SO}^2}+\frac{1}{D\tau_B}\right]^{-\frac{1}{2}} - \frac{1}{2}\left[\frac{1}{l_\phi^2}+\frac{1}{D\tau_B}\right]^{-\frac{1}{2}} \\ &-\frac{3}{2}\left[\frac{1}{l_\phi^2}+\frac{4}{3l_{SO}^2}+\frac{3}{l_e^2}+\frac{1}{D\tau_B}\right]^{-\frac{1}{2}} + \frac{1}{2}\left[\frac{1}{l_{\phi^2}}+\frac{3}{l_e^2}+\frac{1}{D\tau_B}\right]^{-\frac{1}{2}}\Bigg)\end{aligned} \tag{2.15}$$

where, $l_\phi = \sqrt{D\tau_\phi}$ and $l_{SO} = \sqrt{D\tau_{SO}}$.

The correction to the magnetoconductance depends on the ratio of l_{SO} to l_ϕ, which also determines the sign of the modification. That is, when $l_{so} < l_\phi$ an increase in conductance at B = 0 is observed as seen in fig. 2.11 (black line). This trace corresponds to WAL with little or no weak localization (WL). A reduced conductance is observed when $l_{so} < l_\phi$ (red line), which corresponds to WAL with some WL contributing. In the final case a finite l_{SO} results in a reduction

of the weak localization amplitude when compared to the case where spin-orbit interaction is omitted (blue trace).

Fitting of the model in eq. 2.15 to WAL data allows one to extract l_{SO} and l_{ϕ} under the approximation of the nanowire diameter, D. Two general regimes are typically considered, namely, the diffusive and the ballistic. During this thesis only the diffusive regime has been considered.

Sample Fabrication & Experimental Setup 3

This chapter will cover the experimental basics that have been used through-out all the different experiments described in this work. A natural place to start is with the basics of sample preparation. Only a brief description of these processes will be given here. Detailed recipes are provided in the Appendix section 7.1. Next, a description of the dilution refrigerator, where the sample is cooled, will be given. Last, the measurement setup hooked up to the dilution refrigerator and used for data acquisition, will be described.

3.1 Sample Fabrication

This section will briefly discuss the basics of electron beam lithography and Al etching. These two steps cover most clean-room style microchip fabrication processes performed during this work.

3.1.1 Electron beam lithography

Electron beam lithography (EBL) is used to define microscopic patterns of materials that can be evaporated, sputtered or grown. This techniques is one of the most fundamental techniques used in the condensed matter lab where structure resolution

smaller than a few hundreds of nm is desired. The approach discussed here is EBL specifically on semiconductor nanowires. One starts with spin coating a polymeric

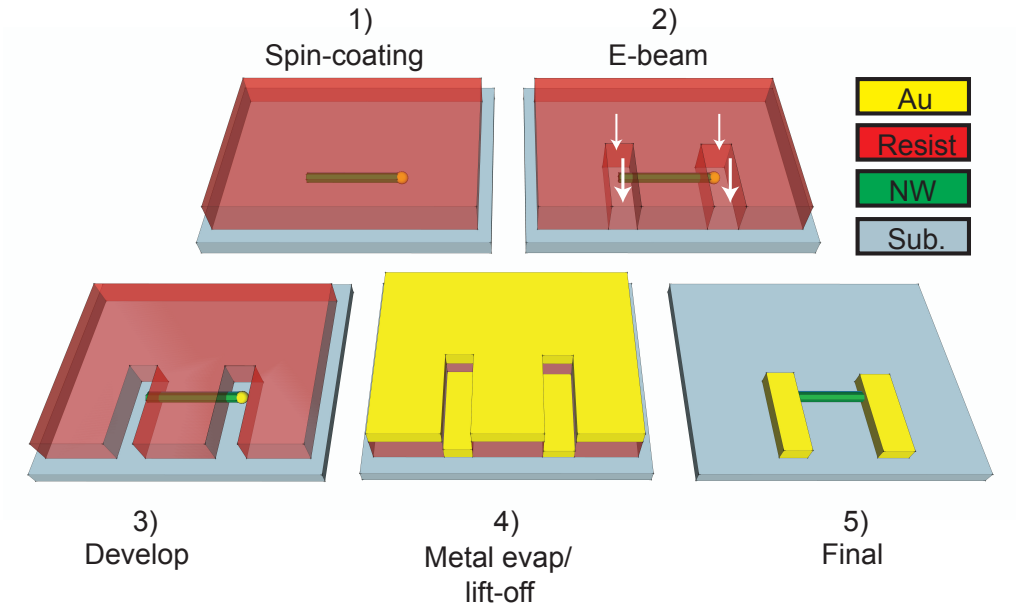

Figure 3.1: The principles of electron beam lithography. The steps are: 1) Spin-coat a electron beam sensitive polymer on the chip already covered in nanowires. 2) Expose desired regions of the polymer to doses of electrons in order to break the polymeric chains to make the certain parts of the polymer susceptible to a developing solution. 3) Develop the exposed parts of the polymer. 4) Deposit a metal (in this case Au is used) onto the whole chip, and let the chip sit in a solvent to lift-off all remaining resist. 5) The final device is ready with Au only covering the areas exposed to the electron beam.

resist (for instance PMMA, A6) onto a degenerately doped Si chip with 100 nm thermal oxide, and baking it at 185°C for 2 min. In our case nanowires are most likely deposited onto the chip prior to this step. Baking the chip hardens the resist, cross-links the polymeric chains and evaporates solvent residues. After a desired design is drawn in a CAD software the chip is loaded into the electron beam system, where the design is exposed in doses of electron shots onto the resist, selectively breaking the polymeric chains. The chip is then developed in a developer solution (MIBK/IPA 1:3), which removes the exposed resist. Next, the sample is loaded into a metal evaporation chamber where the oxide on the

semiconductor nanowire is removed by ionized Ar milling. Hereafter, a layer of Ti (typically 5 nm) is evaporated as a sticking layer, followed by a thicker layer of Au (typically 130 nm). The chip is left in heated acetone (60 °C) in order to remove all remaining resist. This results in a microscopic pattern defined in Ti/Au on the wafer. These 5 principles are sketched in fig. 3.1

3.1.2 Al etching

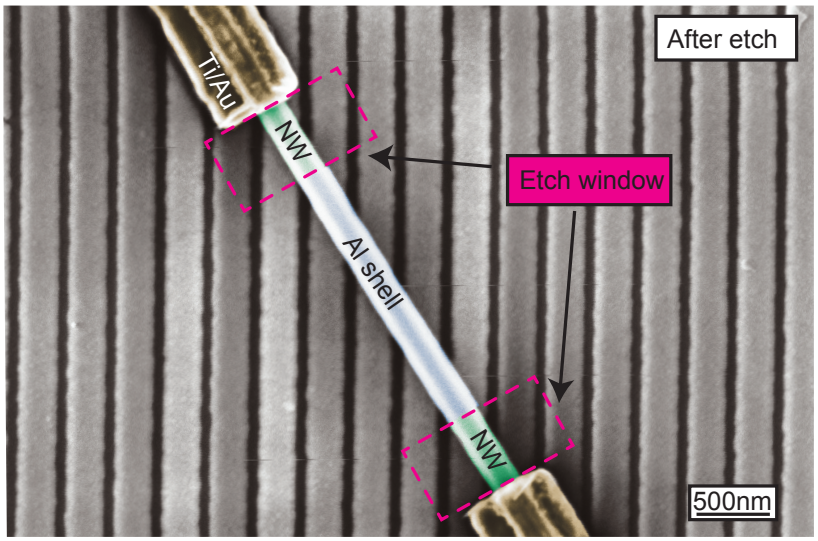

FIGURE 3.2: Selectively removing Al off of nanowires. A nanowire with Al grown on 2 facets is contacted by EBL. After defining etching mesas in the resist, by repeating the EBL procedures from 1 to 3, the nanowires is submersed in Al etchant type D for 10 sec. and thoroughly rinsed in Mili-Q water. This results in selective removal of Al off of the nanowire, as indicated by the 2 red dashed rectangles.

Following the EBL steps 1 through 3 one covers the whole chip in hard baked resist, leaving only selectively chosen windows open for the Al etchant to work. Having performed the EBL procedures, the chip is submersed in 55 °C hot Al etchant Type D for 10 seconds before thoroughly rinsing in large amounts of ultra-pure H_2O (Mili-Q). A typical result can be seen in fig. 7.7.

Experimental setup

This section will concern itself with entirety of the experimental setup used to infer the fabricated nanowire devices. First the basics of the dilution unit is explained, followed by an explanation of the measurement setup used to measure the devices at temperatures of T $\sim$ 20-40 mK.

3.2 The dilution unit

At high temperatures the thermal energy k_BT, where k_B is the Boltzmann's constant and T is the temperature, broadens or completely averages out quantum phenomena. Bringing the thermal energy to a point where the relevant energy scale of the experiment becomes bigger than, $k_BT < E_{relevant}$, is therefore paramount.

The main component of the dilution refrigerator is the dilution unit, see fig. 3.3 **a** for an image of the dilution unit inside the Oxford Instruments dilution refrigerators used in this lab. Generally speaking the cooling effect can be split into two parts: 1) the pre-cool step where a temperature of $\sim$ 10 K on the dilution unit is obtained by circulating a gaseous mix of ^{3}He and ^{4}He trough a circuit that is thermally coupled to the stage holding the mixing chamber by use of a pulse tube cooler. When a temperature of $\sim$ 10 K is reached the next step kicks in. Step 2) relies on the quantum phenomenon that as temperature decreases, the mix of ^{3}He and ^{4}He will never solidify, and that the minimum solubility of ^{3}He in ^{4}He never becomes lower than 6.6 % even for T $\rightarrow$ 0.[28]

This effect relies on the Fermi and Bose statistics of the two elements. Since ^{4}He acts as a Bose condensate the quantum mechanical zero point motion only allows a certain minimum distance between the S = 0 ^{4}He and the spinful ^{3}He. By continuously evaporating and recircling ^{3}He through the ^{3}He and ^{4}He mix continuous cooling power can be maintained in the closed circuit, due to a constantly undergoing phase transition. 5-10 mK is the practical limit due to the thermal coupling to the environment. Placing the sample in thermal contact to the mixing chamber will cool the sample, as seen in fig. 3.3 **b**.

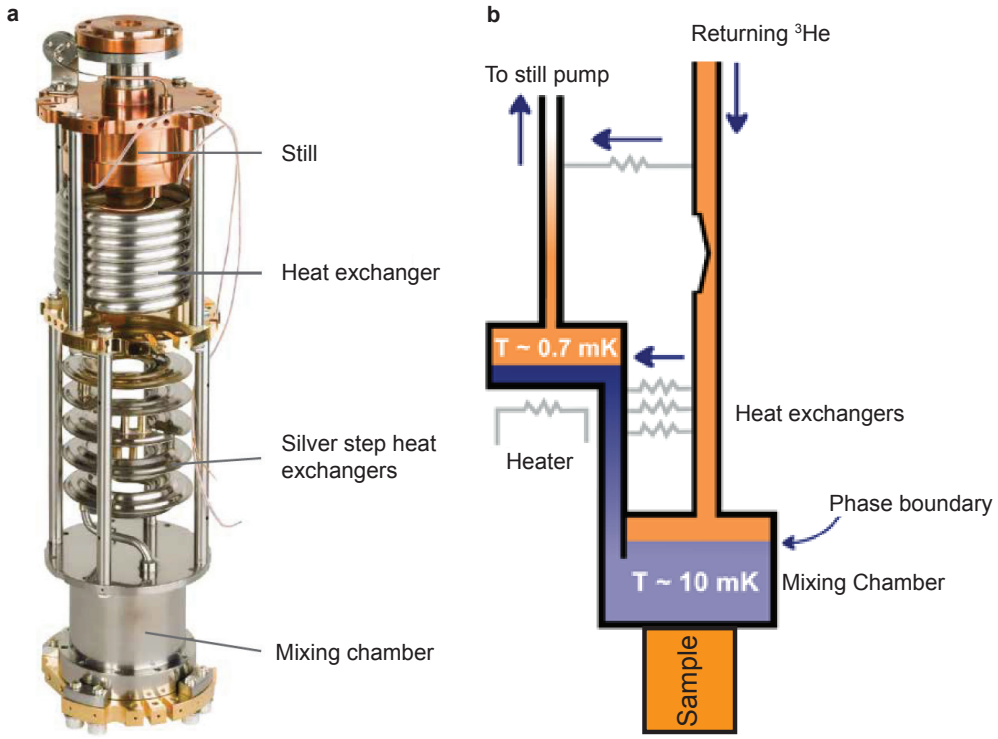

FIGURE 3.3: Principles and example of the modern dilution refrigerator. **a**) Image of modern dilution unit with silver heat exchangers and the most important features of the dilution unit. **b**) From the still the pure ^{3}He is transferred back to the pump for recirculation and repressurizing. The ^{3}He is funneled through a flow impedance securing a steady flow. Heat exchangers cool the the returning ^{3}He and heats the still. The phase boundary indicates the separation of the pure ^{3}He and the "mix" of ^{3}He and ^{4}He with final solubility of 6.6 %. The heater boils of the lighter ^{3}He from the 1 K pot finalizing the loop for the perpetual flow of ^{3}He. This way ^{3}He will constantly undergo a phase transition from the ^{3}He pure phase into the mixed phase providing cooling power on the mixing chamber. The sample loaded into a copper casing (puck) is in thermal contact with the mixing chamber, providing cooling power on the sample. Figures are adapted from Oxford Instruments and slightly modified.[27].

3.3 Measurement setup

This section will explain the basics of the measurement setup used for more or less all devices discussed in this work. Fig. 3.4 shows the circuit diagram of the setup. The AC lock-in signal stemming from a Stanford Research SR830 lock-in amplifier

is merged with the DC signal from the DECA-Digital-Analog-Converter (DAC) in an AC-DC adder and voltage divider. The excitation voltage from the lock-in is divided by the resistor $R_1 = 1\text{M}\ \Omega$ and the ground essentially down-converting the amplitude by a factor 10^6.

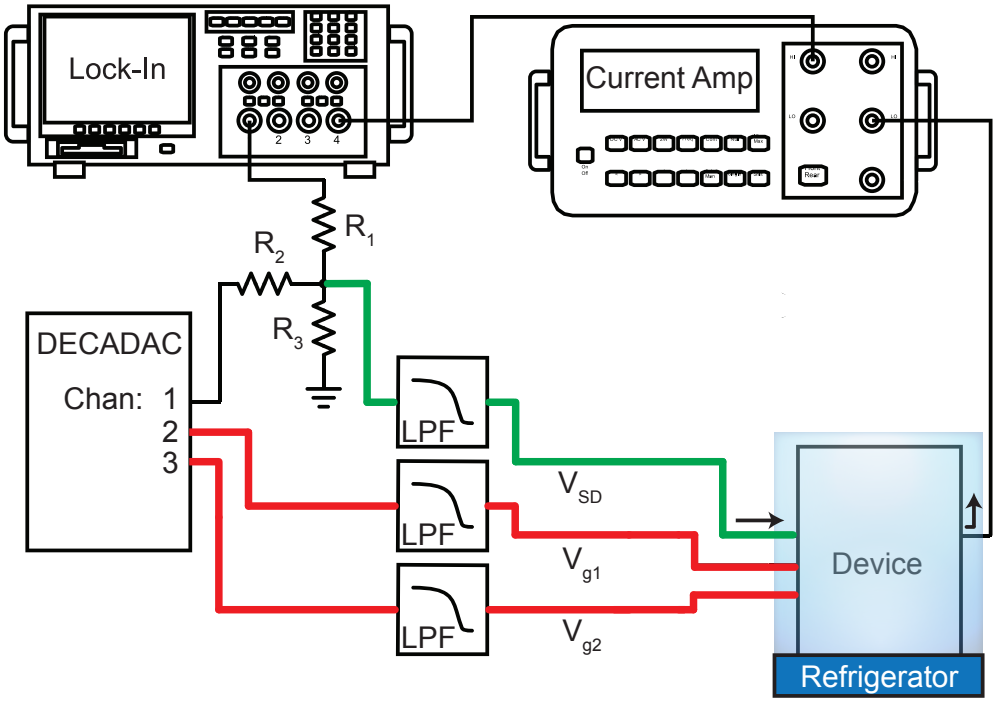

Figure 3.4: The generic experimental setup for lock-in signal detection. The DC signal from the DECADAC and the AC signal from the lock-in (green line) is down-converted by a factor 10^3 and 10^6 by the voltage divider. respectively. The signals are hereafter added and filtered through 1.9 MHz low pass filters (LPF), before reaching the dilution refrigerator to be cooled at different cooling stages before reaching the sample. The AC current is amplified by the current amp and fed back to the lock-in where the applied V_{AC} is digitally divided by the detected I_{AC} converting the signal into differential conductance on top of DC voltages applied from the DECADAC. Additional DC channels on the DECADAC are used to control the electrostatic gates on the device (red lines).

A similar explanation is valid for the DC signal which is fed from the DECADAC and down-converted by $R_2 = 1\text{k}\ \Omega$ and ground. $R_3 = 56.2\ \Omega$ is chosen in order to impedance match. Different AC excitation voltages are used but they generally range from $V_{AC} \sim$ 6-60 μeV which is smaller compared to the energy scale of the

induced superconducting gap of $\Delta \sim 230\ \mu eV$. The lockin frequency is chosen as an odd number, typically 133.3 Hz, as to avoid any 50 Hz or multiples hereof noise from the in-house electrical wiring. The DC signal from the 16 bit DAC is down-converted by a factor 10^3 due to the resolution limit of 0.3 mV[i], in order to avoid operating at the resolution limit. The combined AC and DC signal is shown as the green line in fig. 3.4 the other channels on the DAC are not down-converted and are connected to the gates of the device. These are shown as the red lines. All lines are fed through a low-pass filter (LPF) with a cut-off frequency of 1.9 GHz in order to avoid high frequency noise. The signal outputted from the sample is amplified by a factor 10^7 and split in the current amplifier. The DC signal is recorded in the digital multimeter and the AC signal is detected in the lock-in and digitally converted into the differential conductance g = dI/dV.

[i]The excitation range of the DAC is $\pm 10V$ providing a resolution limit of $20\text{V}/2^{16} = 0.3$ mV.

Spin-Orbit Coupling in InAsSb Nanowires 4

This chapter concerns itself with measurements carried out on an $InAs_{1-x}Sb_x$ nanowire with step-like changes in the ratio between As and Sb and a constant In content. The device geometry is presented followed by 4-probe characterisation and UCF measurements. Finally, WAL measurements are shown from which the spin-orbit length and the phase coherence length are extracted. These values are converted into spin-orbit coefficients α and discussed with respect to the literature. Two identical devices with similar behavior are measured, however, only data from one of the measurements is presented for brevity.

Molecular beam epitaxy (MBE) grown $InAs_{1-x}Sb_x$ are grown axially in the [111] zincblende orientation. An InAs stem is grown at first, hereafter different flux ratios of As and Sb (x = 0.1, 0.2,..., 0.6) are introduced. This results in step-like changes in the Sb concentration along the nanowire axis. The $InAs_{1-x}Sb_x$ nanowires are deposited on degenerate doped highly conducting Si chips with 100 nm thermal oxide acting as an insulator. Regular EBL is used to contact the nanowire with Ti/Au (5nm/120nm) and place gate electrodes. Ionized Argon milling is performed to ensure good ohmic contact to the semiconductor. Differential conductance is measured using standard AC lock-in techniques in a dilution refrigerator with at basetemperature of 20 mK. A scanning electron micrograph of the device is seen

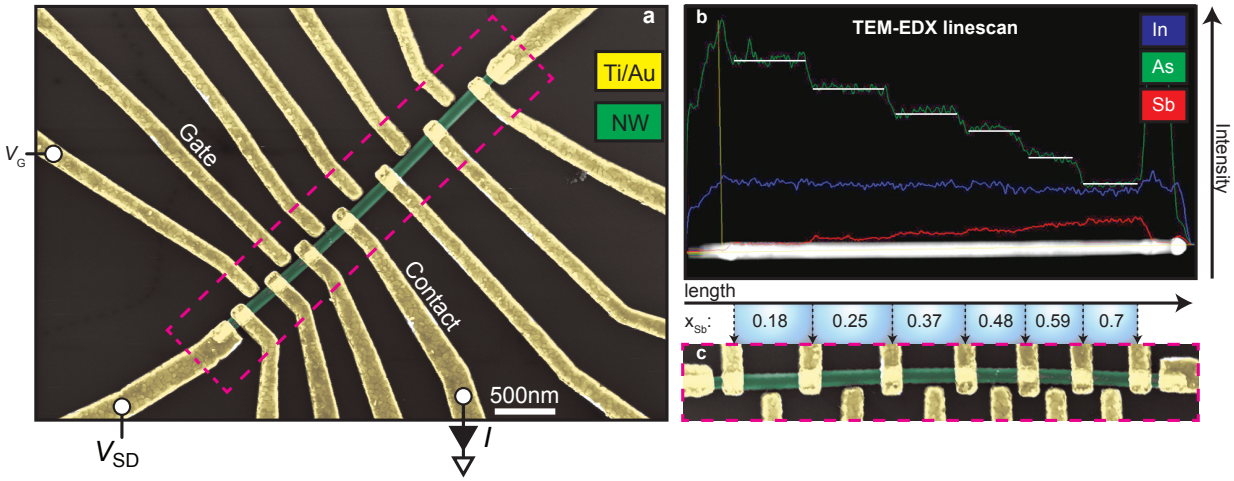

Figure 4.1: The device principles of Spin-Orbit experiment on $InAs_{1-x}Sb_x$ nanowires. **a**) False-colored scanning electron micrograph of the $InAs_{1-x}Sb_x$ nanowire device with 9 contacts and 6 gates. The number of gates and contacts makes it possible to perform 4-probe measurements on every individual segment on the nanowire. Every one of these segments can be gated by a gate electrode in close proximity. Source-drain voltage, V_{SD}; V_G, gate voltage; I, measured current. **b**) The $InAs_{1-x}Sb_x$ nanowire is grown with a step-like change in the Sb molar fraction as verified by EDX line-scans performed in a transmission electron microscope. The step-like changes of the As concentration getting smaller is seen by the white overlay. **c**) Zoom-in of **a** illustrated by a dashed red line. The initial InAs segment and the Au-seed particle used to nucleate growth, as seen in **b**, is matched during the EBL design process to accurately place contacts and gates with respect to the change in Sb molar fraction.

in fig. 4.1 **a**. Every segment of different Sb molar fraction is in close proximity to a side-gate electrode and has at least two contacts on either side of the gate, in order to allow for 4-probe measurements. The segment length and concentration of Sb, x, is determined from energy dispersive x-ray spectroscopy (EDX) performed by Thomas Kanne. In fig. 4.1 **b** a transmission electron micrograph on which an EDX line-scan is performed is evident. The three plotted line-scans display the intensity of a step like decrease in As (green trace), and a step-like increase in Sb (red trace). The intensity of In (blue trace) is constant as expected. Explanations on the extraction of the quantitative Sb molar fractions, the decreasing segment lengths and the low intensity of the Sb EDX trace, is beyond the scope of this

work. The rectangle outlined by the dashed red line as seen in fig. 4.1 **a**, displays a cut-out of the device and its distinct $InAs_{1-x}Sb_x$ nanowire segments in **b**. The length of each segment decreases for higher Sb concentrations which is accounted for during lithography.

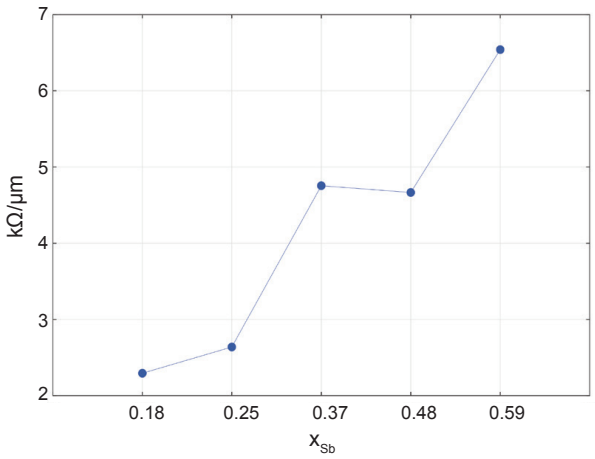

FIGURE 4.2: 4-probe resistances of each $InAs_{1-x}Sb_x$ nanowire segment with changing Sb molar fraction. The length-normalized 4-probe resistance is plotted as a function of Sb molar fraction, x_{Sb}. Evidently the resistance increases for increasing Sb content.

Fig. 4.2 shows the 4-probe resistance normalized for length as a function of Sb concentration[i]. Noticeably the resistance is increasing for increasing Sb concentrations which could be indicative of alloy scattering. For increasing Sb concentration the ternary nanowire could contain more and more randomly placed Sb in the ordered InAs lattice perturbing the potential landscape creating scattering sites to maximum perturbation at x = 0.7 [29], if one assumes similar carrier densities from segment to segment. Unfortunately, nanowires with x > 0.7 were not grown, in order to verify if the resistance will decrease after x = 0.7. Other scattering mechanism, such as inhomogeneity resulting from impurity segregation, formation of clusters in the solid-solution crystals and compositional fluctuations, [30;31;32] could contribute to the increasing resistance.

[i]The last data point is missing due to a broken contact making a 4-probe measurement of the x = 0.7 segment impossible.

4.1 Universal Conductance Fluctuations

Universal conductance fluctuation measurements as described in section 2.3.2 can be observed in microscopic samples whose electronic paths enclose an area and are subjected to magnetic fields. Phase differences between different electronic paths in the sample are dependent on the Fermi velocity. The same interference effect can occur when electron densities are affected by electrostatic gate potentials, and the Fermi velocity thus is altered.

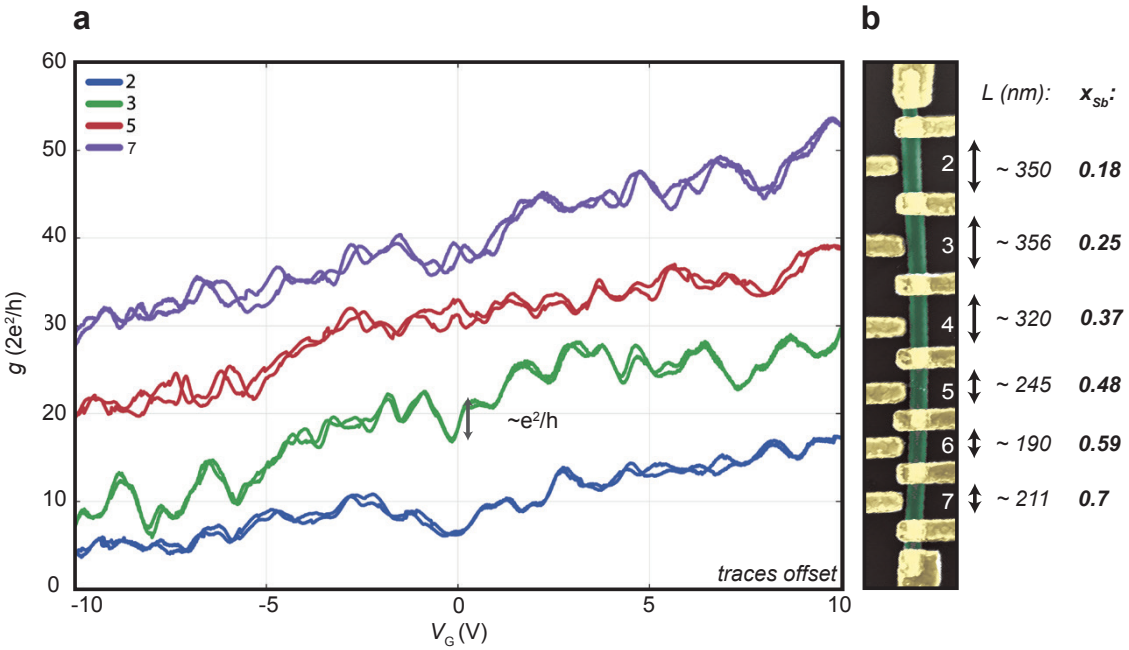

Figure 4.3: Universal conductance fluctuations of magnitude $2e^2/h$ for individual $InAs_{1-x}Sb_x$ nanowire segments. Differential conductance, g is shown as a function of gate voltage V_G. Double traces of segment 2 (blue), 3 (green), 5 (red) and 7 (purple) are shown in according to **b**. All double traces are offset for clarity. The double traces have a high degree of similarity indicating universal conductance fluctuations. The amplitude of the traces are on the order of e^2/h as indicated by the black arrow. **b**) A false colored scanning electron micrograph of the device, its segment numbering and individual length. Since the amplitude of the UCF are $\sim e^2/h$ the phase coherence length, l_ϕ is at least on the order 190-350 nm.

Such conductance fluctuation measurements are evident in fig. 4.3 **a**. Each trace is performed by sweeping the proximal gates from -10V to 10V and back

again. The two traces are plotted on top of each other. It is noted that the repeated traces bear a high degree of resemblance, which is in good agreement with theory stating that UCF are stable and reproducible in time.

If these measurements are indeed due to UCF, theory states that the phase coherence length, l_ϕ, is on the order of or larger than the sample length, if the amplitude of the conductance fluctuations are on the order of e^2/h for $T \to 0$. This is indeed the case as the UCF amplitude, as indicated by the gray arrow in fig. 4.3 **a**, is on the scale of e^2/h. This indicates that the phase coherence length, $l_\phi \sim$ 190-350 nm, since the length of the segments vary from 190-356 nm as seen in fig. 4.3 **b**.

4.2 Magnetoconductance and Weak Antilocalization

Now we turn our focus to magnetoconductance measurements and weak antilocalization. In order to resolve localization effects based on magnetoconductance measurements, conductance fluctuations, or UCF in our case, have to be suppressed sufficiently. Two common approaches have been utilized with success, so far:

- Constantly averaging the conductance of the sample according to the Fermi energy, E_F, will average out the contribution from the conductance fluctuations.[33] This can be effectuated by a constant sweeping of gate electrodes, which is analogous to averaging over multiple of samples with contrasting impurity levels. This is valid for as long as the averaging in E_F is equal to or larger than the characteristic auto-correlation length.[34][ii]

- Measuring on a number of samples connected in parallel, conductance fluctuations from individual samples are averaged out, as demonstrated by Hansen et al.[35] and briefly described above.

The first technique is utilized in the following WAL measurements. An arbitrary wave-form generator with a peak-to-peak voltage of 8 V is connected to the gates

[ii] Auto-correlation is a tool for analysis of repeating patterns. This could for instance entail the presence of a periodic signal obscured by noise. E_F has to be larger than the auto-correlation length to satisfactory average out UCF.

at a frequency of 2 Hz and a time constant of 3 s on the lock-in. The peak-to-peak value is chosen to be $V_{pp} \pm 8$ V in order to average over a sufficiently large number of UCF periods. The low frequency of the wave form generator is chosen in order to provide sufficient charging time of the gate, which is necessary since a large resistor is connected between the wave form generator and the gates[iii]. The time constant on the lock-in of 3 s is chosen in order to allow for sufficient averaging from the wave form generator to be recorded for each data point. Preliminary tests on wave form generator voltage ranges are provided in the Appendix section 7.4.

Two-terminal magnetoconductance measurements are performed on each $InAs_{1-x}Sb_x$ nanowire segment with increasing x, while the UCF are averaged out. The mean value differential conductance as a function of perpendicular magnetic field across the different segments of the $InAs_{1-x}Sb_x$ nanowire is seen in fig.4.4 **a**. The one-dimensional and diffusive regime weak antilocalization model described in section 2.3.6 is fitted to each trace with accordingly different Sb concentration (the red line). For each segment l_ϕ and l_{SO} are extracted and plotted as a function of x as seen in fig. 4.4 **b** and **c**, respectively. The diameter, D, of the nanowires is chosen to be 80 nm for the fit. The other free parameters (l_ϕ and l_{SO}) are chosen as to fit the data. From scanning electron micrographs of the $InAs_{1-x}Sb_x$ nanowire the diameter appears to be $\sim$ 100-110 nm. Uncertainties in these plots are: correct modeling size of the nanowire diameter, and that externally applied voltages are known to modify the spin-orbit interaction in nanowires.[21]

The extracted values of l_ϕ of $\sim$ 140-225 nm seen in fig. 4.4 **b** are comparable to the rough estimates based on the UCF measurements. Differences in extracted phase coherence lengths could be due to fitting uncertainties described above. From similar magnetoconductance measurements on InN nanowires phase coherence lengths of $l_\phi \sim 115$ nm are extracted.[33] These are a little smaller but on the same order of magnitude as the values obtained in this work. The fact that Peterson et al. performed their measurements at T $\sim$ 0.8 K and not at T $\sim$ 30 mK, is probably of little relevance since the magnitude of the phase coherence lengths typically saturates at $\sim$ 1 K.[35] Phase coherence lengths extracted from InAs

[iii] The large resistor serves as a current limiter to the sample if a gate leak should suddenly occur.

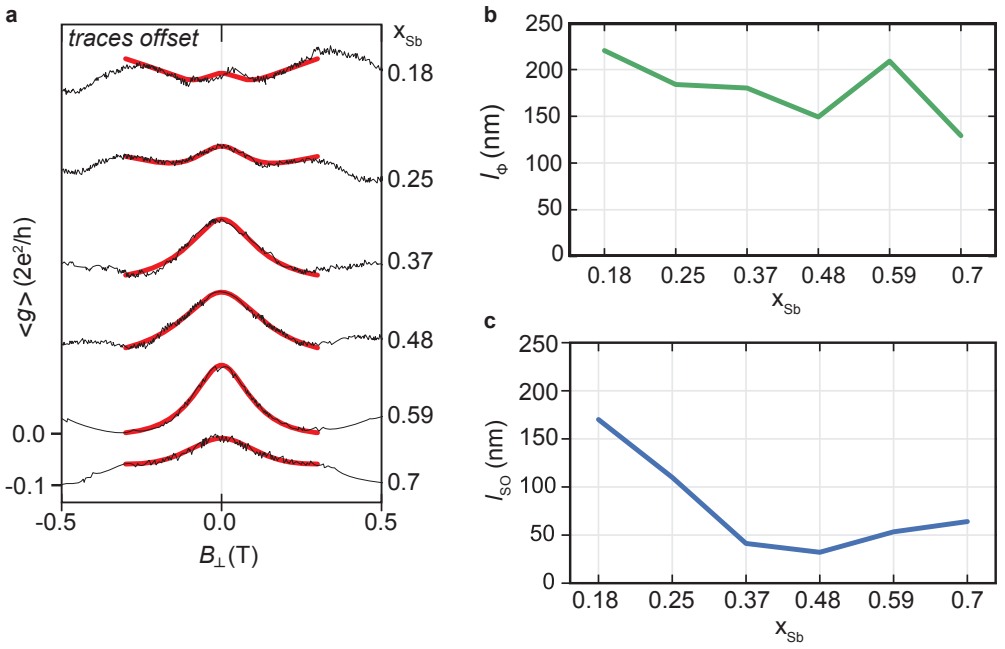

FIGURE 4.4: Fitting magnetoconductance traces for individual $InAs_{1-x}Sb_x$ nanowire segments. **a**) Mean value differential conductance, $< g >$, as a function of perpendicular magnetic field $B_\perp$ is shown for different molar fraction of Sb. The UCF is suppressed by a 2Hz oscillating gate voltage $V_{pp} = 15$ V. The traces are offset for clarity. The peaks at $B_\perp = 0$ show weak-antilocalization behavior. Each WAL trace for each individual Sb molar fraction is fitted with the diffusive limit model. From this the phase coherence length, l_ϕ, and spin-orbit length, l_{SO}, is extracted for each Sb molar fraction and plotted in **b** and **c**. **b**) l_ϕ as a function of Sb molar fraction. Phase coherence lengths of the order $\sim$ 140-225 nm are extracted. **c**) Spin-orbit length, l_{SO}, as a function of Sb molar fraction is plotted. The range of $l_{SO} \sim$ 35-160 nm. A minimum of $l_{SO} = 35$ is obtained for x = 0.48.

nanowires[35] yield a l_ϕ of 260 nm. Additionally, $l_\phi = 300$ nm is found in InAs nanowires.[36] Taking literature into account, it is found that the phase coherence lengths extracted in this work are realistic.

The spin-orbit length, l_{SO}, as a function of x, plotted in fig. 4.4 **c**, exhibits a clear decrease in l_{SO} for increasing x to a minimum at x $\sim$ 0.48. For x $>$ 0.48 l_{SO} increases again. The values for l_{SO} range from 160 nm to 35 nm, where l_{SO} at x $\sim$ 0.48 is approximately half the magnitude of the smallest l_{SO}, that could be found in literature when comparing to InAs and InSb nanowires.

For InAs nanowires the smallest l_{SO} found is on the order of 50-70 nm.[36;21] For InSb nanowires an $l_{SO} \sim 100$ nm is found.[37] The $l_{SO} = 50$ nm found in InAs nanowires should be treated with caution since their measurements were performed at finite backgate voltages of 30 V, and finite electrostatic fields are known to modify spin-orbit interactions[iv].[21]

It should be noted that the same minimum $l_{SO} \sim$ 30-40 nm at x $\sim$ 0.48 remains constant for many V_{pp} ranges which suggests that the low l_{SO} is indeed a robust phenomenon and not an artifact. The other averaging voltages are seen in Appendix section 7.4.

4.3 Rashba spin-orbit coefficients

The spin-orbit length l_{SO} is linked to the Rashba spin-orbit coefficient, α, based on the relationship[21],

$$\alpha = \frac{\hbar^2}{2m^* l_{SO}}, \tag{4.1}$$

where $\hbar$ is the reduced Planck's constant and m^* is the effective mass. For conversion of l_{SO} into α the individual effective electron mass for each segment is found by means of table values.[38] The applied effective electron mass values range form 0.0287 to 0.033 m_e values, where m_e is the effective electron mass.

As seen in fig. 4.5 **a** α is plotted as a function of x. The Rashba coefficient exhibits a maximum at x $\sim$ 0.48. Extrapolating α to values for pure InAs and InSb, it is found that the values are comparable.[37;21;36] Any differences could be explained by fit uncertainties, because larger nanowire diameters will result in a smaller l_{SO} and vice versa. Additional differences could be attributed to different l_{SO} to α conversion techniques.[37;21]

In a theoretical proposal by Winkler et al.[39] it is hypothesized how the spin-orbit splitting in $InAs_{1-x}Sb_x$ nanowires as function of x = 0 to 1 will behave. See fig. 4.5 **b**. They propose that α is maximized for x $\sim$ 0.6. The calculations are based on asymmetries in randomly alloyed InAsSb supercells. The data seen in **a**

[iv] The Rashba coefficient is inverse proportional to l_{SO}.[21]

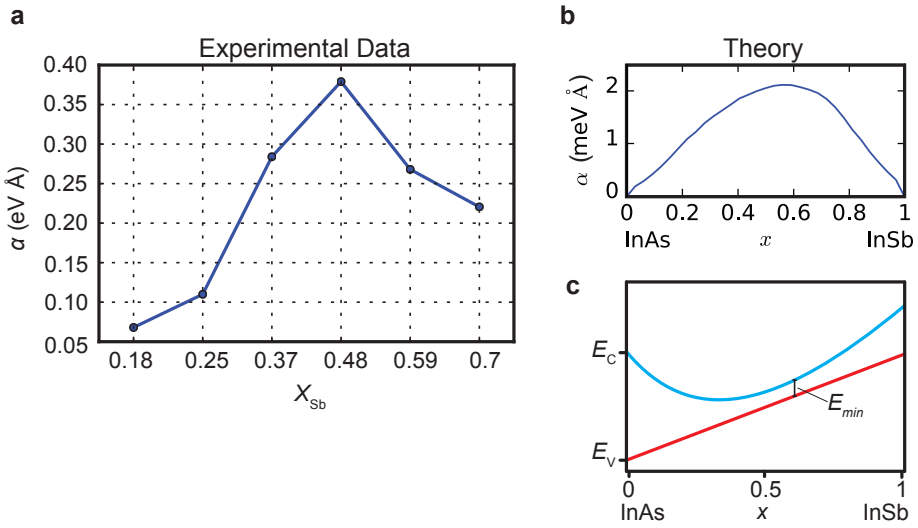

FIGURE 4.5: Rashba coefficients in $InAs_{1-x}Sb_x$ nanowires at different x. **a**) Rashba coefficient α extracted from l_{SO} and effective mass, m^*, plotted as a function of Sb molar fraction. Rashba coefficients range from 0.07 to 0.38 eV dependent on x. The maximum α is found for an Sb molar fraction of x = 0.48. **b**) Theoretical proposal by Winkler et al.[39] where crystal asymmetries in supercells of $InAs_{1-x}Sb_{Sb}$ with x = 0 to 1 have sizeable Rashba cofficients for small supercells. α is plotted as a function of x. A noticeable maximum at $x = 0.6$ is observed. The supercell size used here is 64 atoms. The similarity between the experiment (**a**) and the theory (**b**) is most unlikely unless one assumes the electron wavefunction in these nanowires to live an a cylindrical shape. **c**) Plot of conduction and valence band of $InAs_{1-x}Sb_x$ in the whole range $x = 0$ to 1, adopted from Winkler et al.[39] and modified. The bandgap minimum E_{min} is smallest at x $\sim$ 0.6 where one could expect the highest valence to conduction band coupling, resulting in large Rasha coefficients due to larger internal electric fields.

shows a similar trend to what found by Winkler et al., with the difference that the maximum α is not at x $\sim$ 0.5 but at 0.6. The supercells used in the theoretical calculations consist of 64 atoms. As the increase in α already averages out at supercells consisting of 1728 atoms, as the authors discuss, the contribution due to crystal asymmetry is most likely negligible. This work, however, hypothesizes that if the electrons only interact with the nanowire crystal at the surface, similarly to the shape of a cylinder, contributions to α from crystal asymmetries could be non-zero. This model has been used before in theoretical calculations on the

Rashba effect in InAs nanowires.[40]

However, the energy scale of the theoretical proposal is still small compared to the magnitude of the α's found in this work. A different explanation could be given if one considers fig. 4.5 **c**[v]. Here, the conduction band and valence band of an $InAs_{1-x}Sb_x$ nanowire for x ranging from 0 to 1, is seen. At x $\sim$ 0.6 the bandgap E_G is at its minimum, $E_G = E_{min}$. Interestingly, as discussed by Lassnig et al.[41] the Rashba spin splitting in conduction bands result from electric fields in the valence band. It is thus expected that the valence band-conduction band coupling and hence its inter-electric field, is strongest at x = 0.6. Since the electric field coupling is inverse-proportional to l_{SO}, it could be hypothesized that a larger spin-orbit interaction would arise at x $\sim$ 0.6.[42]

We now change our focus to the list of criteria for realization of Majorana fermions in the solid-state as described previously. Large spin-orbit splitting is a crucial ingredient in order to secure robust topological phase transitions[vi].[10] The findings of this chapter indicate that InAsSb nanowires could provide stronger Rashba coefficients, compared to conventionally applied binary InAs and InSb nanowires.

[v] This figure is adopted from Winkler et al.[39] and modified for clarity.

[vi] Recall that the Majorana Hamiltonian contains the Rashba coefficient α

Majorana zero modes in InAsSb nanowires 5

In this chapter, we apply the two Majorana zero mode spectroscopy methods introduced in section 2.2, namely Coulomb spectroscopy and tunneling spectroscopy. Both spectroscopy methods are applied on an $InAs_{0.2}Sb_{0.8}$ nanowire with Al grown on two facets of the nanowire. First, the tunneling device is introduced where the proximitized superconductivity of the Al is inferred, followed by extractions of the g-factor. Next, sub-gap Andreev Bound States (ABS) are detected and evolved in a parallel magnetic field in order to further investigate the Landé g-factor, and show the first signs of a Majorana zero mode in the $InAs_{0.2}Sb_{0.8}$ nanowires. Further measurements exhibit higher order ABS merging and splitting, as well as an anti-crossing of two ABS. Finally, the signature of an additional Majorana zero mode is shown in a different gate configuration in order to underline the robustness of these modes. The next section of this chapter introduces the Coulomb charging device. Here, the spacing between Coulomb resonances as a function of parallel magnetic field shows a transition from $2e$ to $1e$. This is the second signature of a Majorana zero mode in $InAs_{0.2}Sb_{0.8}$ nanowires, provided in this work.

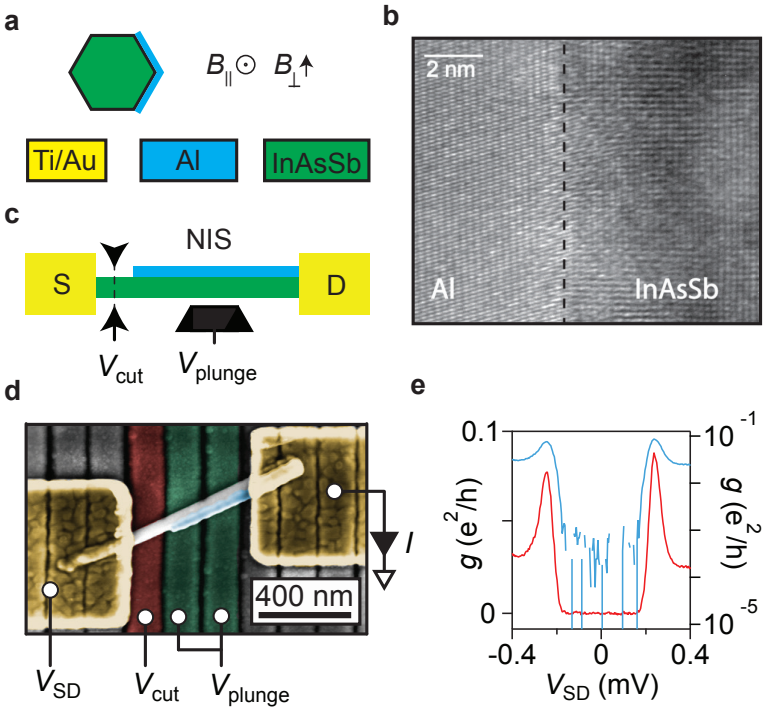

Figure 5.1: Tunneling spectroscopy in a *Delft* device. **a**) Cartoon of the nanowire cross-section with according coloring scheme. Normal metal leads are yellow, the superconducting Al is blue and the $InAs_{0.2}Sb_{0.8}$ nanowire is green. The parallel orientation of the magnetic field is along the nanowire axis. **b**) Transmission electron micrograph of the superconductor/semiconductor interface. Image courtesy Thomas Kanne. **c**) The layout of the device starting from left: Normal metal lead (N) connected to a bare $InAs_{0.2}Sb_{0.8}$ nanowire section. In close proximity to the bare nanowire section the V_{cut} gate is used to create the tunneling barrier (I). The Al shell is grown on 2 facets of the nanowire which is contacted by another normal metal lead (S). This constitutes the NIS device. The V_{plunge} gate tunes the density of charge carriers in the proximitized nanowire segment. **d**) Scanning electron micrograph of the bottom gated *Delft* device. V_{cut}, red; V_{plunge}, green; V_{SD}, source drain voltage; I, measured current. **e**) Differential conductance as a function source drain voltage, V_{SD}, shows a near zero sub-gap conductance. The y-axis for the red trace is linear, and logarithmic for the blue trace.

5.1 Tunneling Spectroscopy of Majorana Zero Modes

MBE grown $InAs_{0.2}Sb_{0.8}$ are grown axially in the [111] zincblende orientation. After the nanowires have grown to lengths of some microns, the sample is tilted

and Al is grown on two of the six facets, resulting in a epitaxially matched and impurity free semiconductor/superconductor interface. A cartoon of the nanowire cross-section illustrating the hybrid material geometry, is seen in fig. 5.1 **a**. In fig. 5.1 **b** a high-resolution transmission electron micrograph of the interface is seen.

The core-shell $InAs_{0.2}Sb_{0.8}$ nanowires are deposited on prefabricated bottom electrodes covered in 14 nm of HfO_x. A selective Al etchant is used to remove Al, before the Al shell and nanowire core is contacted by depositing Ti/Au (5/130nm). To ensure good ohmic contacts ionized Argon milling is performed just prior to metal evaporation. See fig. 5.1 **c** for the schematics of the *normal-insulator-superconductor* (NIS) tunneling device. The gate denoted V_{cut} is used to establish a tunnel coupling of the source to the proximitized segment, whereas, V_{plunge}, controls the chemical potential of the proximitized segment. In fig. 5.1 **d** a false-coloured scanning electron micrograph of the measured device is seen. Differential conductance is measured using standard AC lock-in techniques in a dilution refrigerator with at basetemperature of 30 mK.

The NIS geometry is established by tuning V_{cut} such that the device is in the tunneling regime ($g < g_0 = 2e^2/h$). At B = 0 the device exhibits clear signs of an induced superconducting gap as seen in fig. 5.1 **e**. Here, the conductance is completely suppressed symmetrically around $V_{SD} = 0$, and strong coherence peaks at $V_{SD} = \pm$ 230 μeV are seen. The gap size, Δ, is a slightly larger compared to the Δ = 190 μeV found in similar tunneling experiments on proximitized InAs nanowires.[43] On the left y-axis the differential conductance is plotted linearly (red trace) and on the right y-axis the differential conductance is plotted on a logarithmic scale, showing the differential conductance on the order of the background noise within the gap.

Similar to the experiments performed by Chang et al.[43] on proximitized InAs nanowires sub-gap resonances (SGR) as a function of V_{plunge} are observed as seen in fig. 5.2 **a**. Normal regime conducting superconducting coherence peaks move and anti-cross within the gap changing the conductance magnitude considerably. The SGRs are attributed to either Yu-Shiba-Rusinov (YSR) states or ABS which have been extensively studied.[44;45;46;47;48] YSR states, where one of them is indicated by a green dot, is most likely due to an unintentional quantum dot formed in the

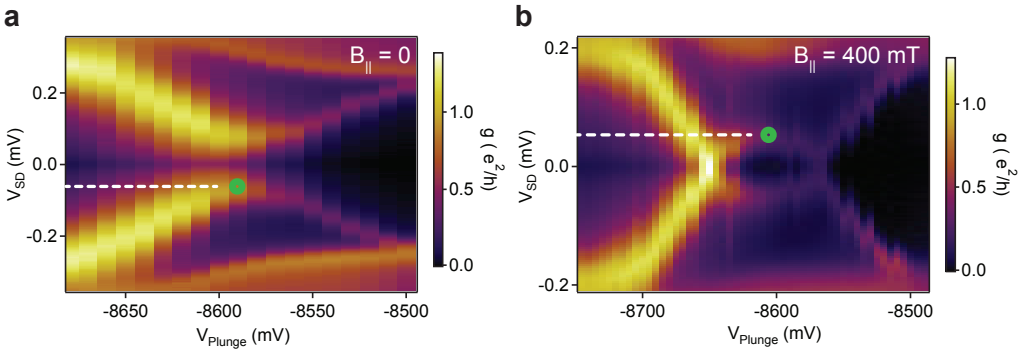

Figure 5.2: Yu-Shiba-Rusinov states in the *Delft* device. Differential conductance as a function of V_{plunge} and source drain voltage V_{SD} in a parallel magnetic field of $B_{\parallel} = 0$ and 400 mT. **a**) $B_{\parallel}$ 0. A quantum dot state likely formed in the tunnel constriction. The YSR state is indicated by a green dot. **b**) $B_{\parallel} = 400$ mT. The shifted YSR is indicated by the green dot. From the energy difference, Δ E = 0.125 meV, a g-factor of 5-6 is extracted.

bare semiconductor segment, similar to previous reports.[43] When the states are evolved in a parallel magnetic field the position of the state moves, as seen in fig. 5.2 **b**, and indicated by a green dot. The differential conductance, g, as a function of V_{SD} and V_{plunge} at a magnetic field of $B_{\parallel} = 400$ mT, is seen. The shift in energy over $B_{\parallel} = 400$ mT, corresponds to the Zeeman energy, $\Delta E_Z = 0.125$ meV. The Zeeman energy,

$$E_Z = g\mu_B B \tag{5.1}$$

where μ_B is the Bohr magneton, g is the Landé g-factor and B is the magnetic field magnitude, allows the extraction of the g-factor for this device on the order of $\sim$ 5-6.

Fig. 5.3 **a** shows differential conductance as a function of V_{SD} and V_{plunge} where a pair of ABS appear and disappear as a function of V_{plunge}, accordingly explained in section 2.2.1. The device is tuned into a slightly different gate configuration as to steer clear of the unintentional quantum dot formed in the tunnel barrier.

Fig. 5.3 **b** shows the gate configuration of the indicated (white line) where ABS are evolved in a parallel magnetic field. Here, differential conductance is plotted

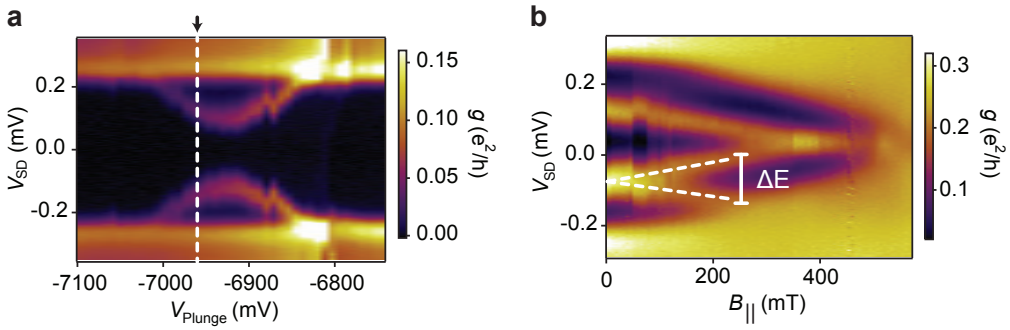

FIGURE 5.3: ABS and Majorana zero modes. **a**) Differential conductance as a function of V_{plunge} and source drain voltage, V_{SD}. ABS evolve in and out of the superconducting coherence peak by tuning the states in the proximitized segment, by V_{plunge}. The white dashed line indicates at which position the ABS are evolved in parallel magnetic field. **b**) Differential conductance as a function of V_{SD} and $B_{||}$. The ABS as indicated in **a** move and merge at E = 0, forming a zero bias peak. This is an indication of a Majorana zero mode. From the Zeeman splitting indicated by ΔE a Landé g-factor of 10 is found.

as function of V_{SD} and parallel magnetic field. The ABS merge and form a peak at E = 0 and $B_{||} \sim 300$ mT. The zero bias peak prolongs for a remaining 200 mT before the superconducting gap closes. This is as a first ever report of Majorana zero modes in InAsSb nanowires. From the Zeeman splitting a g-factor of ~ 10 is found. Other parallel magnetic field traces are plotted in Appendix section 7.2 where g-factors ranging from 6 - 17 are found.

In a different gate configuration higher order ABS can be resolved from the superconducting coherence peaks by evolving in a parallel magnetic field, as seen in fig. 5.4 **a**, where differential conductance is plotted as a function of V_{SD} and parallel magnetic field. At least two distinguishable excited ABS merge and cross when subjected to a magnetic field until the closing of the superconducting gap between 750 mT and 1T. Additionally, avoided level crossings are rare but can be found, as seen in fig. 5.4 **b**, where conductance as a function of V_{SD} and parallel magnetic field is plotted. This peculiarity can be understood as the chemical potential μ outside of the proximitized segment having a positive non-zero value, potentially arising from a coupling of the nanowire to the metallic leads. This essentially makes $\mu \neq 0$ at the end modes of the nanowire, causing the anti-crossing.[49]

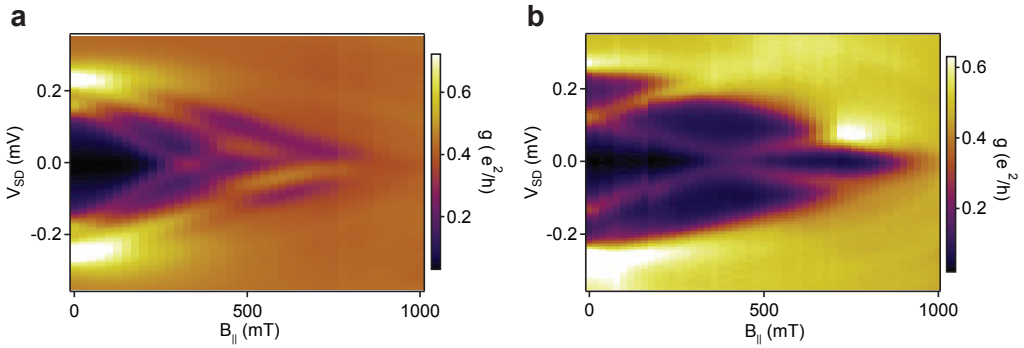

Figure 5.4: Higher order ABS and an anticrossing. **a**) Differential conductance, g, as a function of V_{SD} and $B_{\parallel}$. Higher order ABS merge and cross in a parallel magnetic field. **b**) ABS start to move closer to E = 0, and instead of merging at E = 0, they anti-cross. This could be an indication of non-zero chemical potential μ at the ends of the nanowire.

As a last plot of this section, an additional pair of ABS, found at a completely different gate configuration, are evolved into a Majorana zero mode as seen in fig. 5.5. This figure is shown as to stress the fact that this is indeed a robust system for hosting Majorana zero modes. The ABS displayed in fig. 5.5 **a** reside at considerably less negative $V_{plunger}$ values and at V_{cut} = -9 V.

This is opposed to the gate configuration seen in fig. 5.3 where $V_{plunge} \sim$ -7 V and V_{cut} = -3.5 V . The stronger negative potential on the V_{cut} gate increases the barrier height explaining the lowered differential conductance. The dashed white line indicates the gate configuration where the magnetic field trace shown in 5.5 **b** is initiated. Here, differential conductance as a function of V_{SD} and parallel magnetic field $B_{\parallel}$ shows ABS moving towards E = 0 and merging at $B_{\parallel} \sim$ 380 mT. The zero bias peak remains pinned to E = 0 until closing of the superconducting gap at $B_{\parallel} \sim$ 800 mT. A profile-cut performed along the dashed white line in fig. 5.5 **b** is presented in 5.5 **c**, where differential conductance as a function of V_{SD} is shown. At T $\rightarrow$ 0 and very small excitation voltages theoretical work [50] predicts that the magnitude of the zero bias peak is to be on the order of $2e^2/h$. This is two orders of magnitude larger than what is observed in fig. 5.5 **c** and 4 times larger than what is seen in fig. 5.3 **b**. This difference is attributed to the fact that these experiments were performed at finite temperatures using non-zero excitation

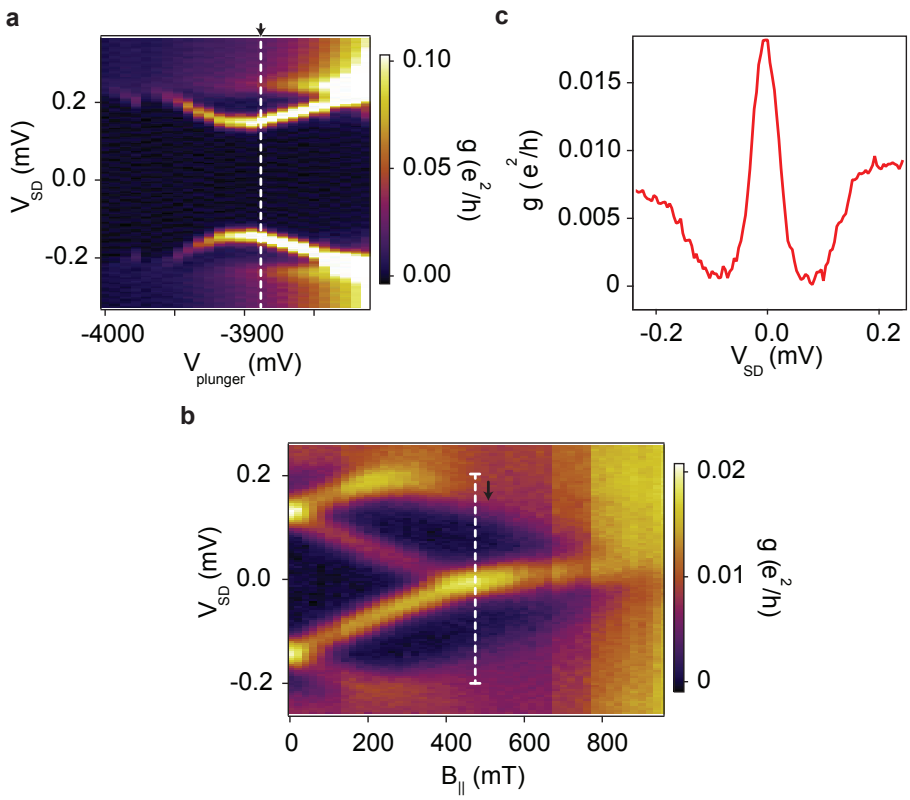

FIGURE 5.5: Majorana zero modes in a different gate configuration. **a**) Differential conductance, g, as a function of V_{plunge} and V_{SD} shows two ABS. These are evolved in a parallel magnetic field $B_{\|}$ in **b** from the position indicated by the white dashed line. **b**) The two ABS states move towards E = 0 and merge at $B_{\|}$ = 390 mT forming a zero bias peak. **c**) Line-cut from **b** showing differential conductance as a function of V_{SD} indicating a zero bias peak height of ~ 0.017 e^2/h. This is more than 2 orders of magnitude lower than what is theoretically proposed.

voltages and that the length of the nanowire is not infinitely long, in order to sufficiently delocalize the zero mode as to prevent Majorana wave-function overlap.

We now change the focus and summarize the experimental data presented so far, taking into account the large spin-orbit interaction in $InAs_{1-x}Sb_x$ alloys as proposed by Winkler et al. and experimentally investigated in this work. The spin-bands in the $InAs_{0.2}Sb_{0.8}$ nanowire are shifted in momentum space as described in section 2.1.2. The magnitude of the shift is expected to be on the spin orbit scale

of $\frac{\alpha^2 m^*}{2\hbar^2} \sim 75$ μeV. This estimate is based on an extrapolated α for $InAs_{0.2}Sb_{0.8}$ nanowires from fig. 4.5 and m* found from table values.[38] The found spin orbit scale is 1.5 times larger than the Majorana zero modes found by Mourik et al.[13], where InSb nanowires were used.

The condition for a topological phase is

$$E_Z > (\Delta^2 + \mu^2)^{1/2}. \tag{5.2}$$

At the ends of the nanowire the electron density will drop to zero, hence μ will sink below the subband levels making μ^2 large. Now, where $E_Z = (\Delta^2 + \mu^2)^{1/2}$ Majoranas zero modes will emerge at each ends of the nanowire. Taking into account the g-factors of the order of $\sim 5 - 17$, the extrapolated $\alpha \sim 0.2$ eV·Å, E_Z/B is found to be on the order of 0.35 - 1 meV/T. From this, it is expected that the transition into the topological phase should appear between 0.23 and 0.73 T. And indeed a zero bias peak at $B_{\|} \sim 300$ mT in fig. 5.3 **b** and at $B_{\|} \sim 380$ mT for 5.5 **a** is observed. Both zero bias peaks stick to, and do not oscillate around E = 0, before the closing of the superconducting gap - evidence of a highly protected topological phase.[49]

Based on the difference between the zero bias peak and the continuum $\Delta_T = 0.1$ meV as seen in fig. 5.3 and the extrapolated α, the superconducting coherence length, ζ, can be found from the relationship,

$$\zeta \approx \alpha/\Delta_T.$$

Here, a ζ of ~ 200 nm is found which fits with experimental fits from Coulomb spectroscopy of Majorana zero modes in proximitized InAs, providing evidence of a protected state.[14]

5.2 Coulomb Spectroscopy of Majorana Zero Modes

We now turn our focus away from tunneling experiments and on to charging experiments, i.e. Coulomb spectroscopy of Majorana zero modes. The same MBE grown $InAs_{0.2}Sb_{0.8}$ nanowires grown axially in the [111] zincblende orientation as in the tunneling experiment are utilized here. The InAsSb/Al nanowires are deposited on highly doped Si covered in 100 nm thermal oxide acting as an insulator.

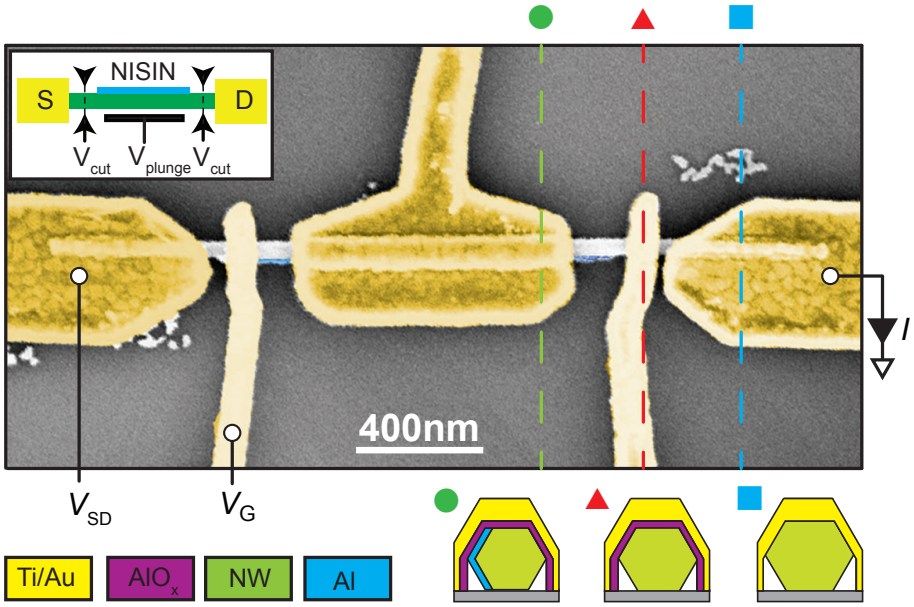

FIGURE 5.6: False-coloured scanning electron micrograph of the top-gated *Copenhagen* device. Yellow, Ti/Au contacts; green, $InAs_{0.2}Sb_{0.8}$ nanowire; blue, two-facet Al; purple, AlO_x. V_{SD}, applied bias voltage; I, measured current; V_G, gate voltage. Three differently colored line-cuts show three cross-sections of the device structure. Green circle is the structure of the Ti/Au top-gate isolated from the nanowire with an Al shell by AlO_x. Red triangle is the structure of the Ti/Au top-gate isolated from the nanowire by AlO_x. Blue square is Ti/Au contacts to the nanowire. Inset: Schematic illustration of the *Copenhagen* geometry.

Selective Al etchant is applied to form an isolated Al island on the $InAs_{0.2}Sb_{0.8}$ nanowire, whereafter the bare nanowire segments are exposed to ionized Ar milling before they are contacted by metal evaporation of Ti/Au (5/120 nm). Argon ion milling is applied to secure transparent contacts to the nanowire. The top-gate dielectric is constructed by repeatedly depositing 0.5-1 nm of Al and oxidizing

the Al in atmospheric air, creating an AlO_x dielectric. Schematics of the *normal metal-insulator-superconductor-insulator-normal metal* (NISIN) geometry and false coloured SEM image of the top-gated device of length $L = 1\mu$m, is seen in fig. 5.6. Differently coloured dashed lines indicate the cross-sectional views of the device in order to illustrate the material layering constituting the top-gates. Differential conductance is measured using standard AC lock-in techniques in a dilution refrigerator with a basetemperature of 30 mK.

As seen in fig. 5.7 **a** the differential conductance, g, as a function of V_G at $V_{SD} = 0$, shows near evenly spaced Coulomb resonances. Tuning V_G of a semiconductor quantum dot, its occupation can be tuned by from $E(N)$ to $E(N \pm 1)$, where N is the integer number of electrons on the island. By changing the electrostatic potential on the capacitively coupled V_G, the charge on the island is changed with the quantized amount e.[51] However, since the island is proximitized, it is expected that only tunneling of Cooper pairs of charge $2e$ is allowed for energies $eV_{SD} < \Delta$. To verify this, a second parameter, namely the source drain bias, V_{SD} needs to be accounted for.

Differential conductance as a function of V_{SD} and V_G is seen in fig. 5.7 **b**, where a Coulomb diamond within Δ is evident. The distance between two coulomb Diamonds within Δ is double the distance of Coulomb resonances seen above Δ. This is comparable to literature where a two e periodic Andreev current has been observed in superconducting metallic islands, with the same doubled charging periodicity above-gap.[18] The same has recently been observed in proximitized InAs nanowires.[52;14]

A noticeable negative differential conductance is observed at higher bias-voltages, attributed to a slowed escape of quasiparticles blocking transport.[52] A line-cut following the green dashed line in fig. 5.7 **b** is plotted as differential conductance as a function of V_{SD} in **c**. Here, the magnitude of the negative differential conductance is significantly larger than what is observed by Higginbotham et al., which could be due to even slower quasiparticle escapes. The proximitized supercurrent in the $InAs_{0.2}Sb_{0.8}$ nanowire is plotted in fig. 5.7 **d** where suppressed differential conductance is seen symmetrically around $V_{SD} = 0$. Two faint coherence peaks can be seen at $\pm$ 0.12 mV. The trace corresponds to the red dashed

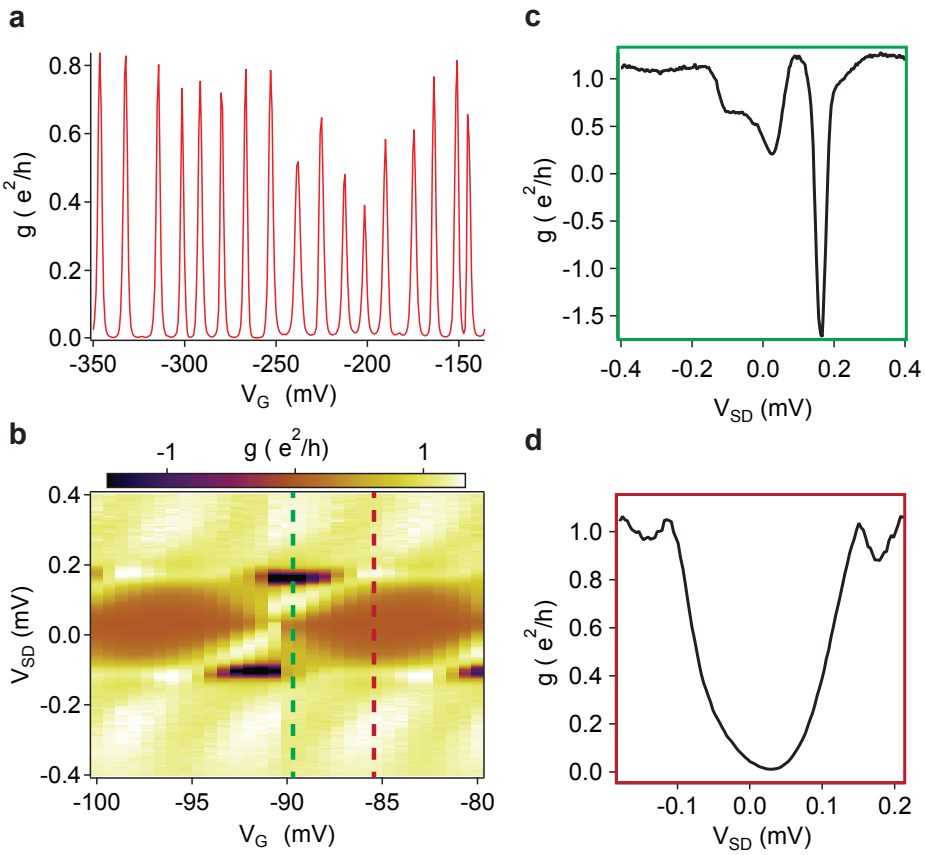

FIGURE 5.7: Coulomb oscillations. **a**) Differential conductance, g, as a function of V_G shows evenly spaced Coulomb oscillations. **b**) Differential conductance, g, as a function of V_G and V_{SD} shows a Coulomb diamond within the superconducting gap, Δ. At $E > \Delta$ Coulomb resonances of half the spacing as within the superconducting gap is visible. A large negative differential conductance is observed for higher bias voltages within the Coulomb diamond. The high negative differential conductance is quantified in the green line-cut seen in **c**. **c**) Differential conductance, g, as a function of V_{SD} shows the magnitude of the negative differential conductance on the order of -1.5 e^2/h. **d**) The red line-cut shown in **b** shows a proximitized gap which has some sup-gap conductance between the two superconducting coherence peaks.

line in fig. 5.7 **b**.

As seen in fig. 5.8 **a** differential conductance as a function of V_{SD} and V_G, shows a series of evenly spaced Coulomb diamonds at a parallel magnetic field magnitude of $B_{\parallel} = 0$. At $B_{\parallel} = 150$ the Coulomb diamonds are still observed and

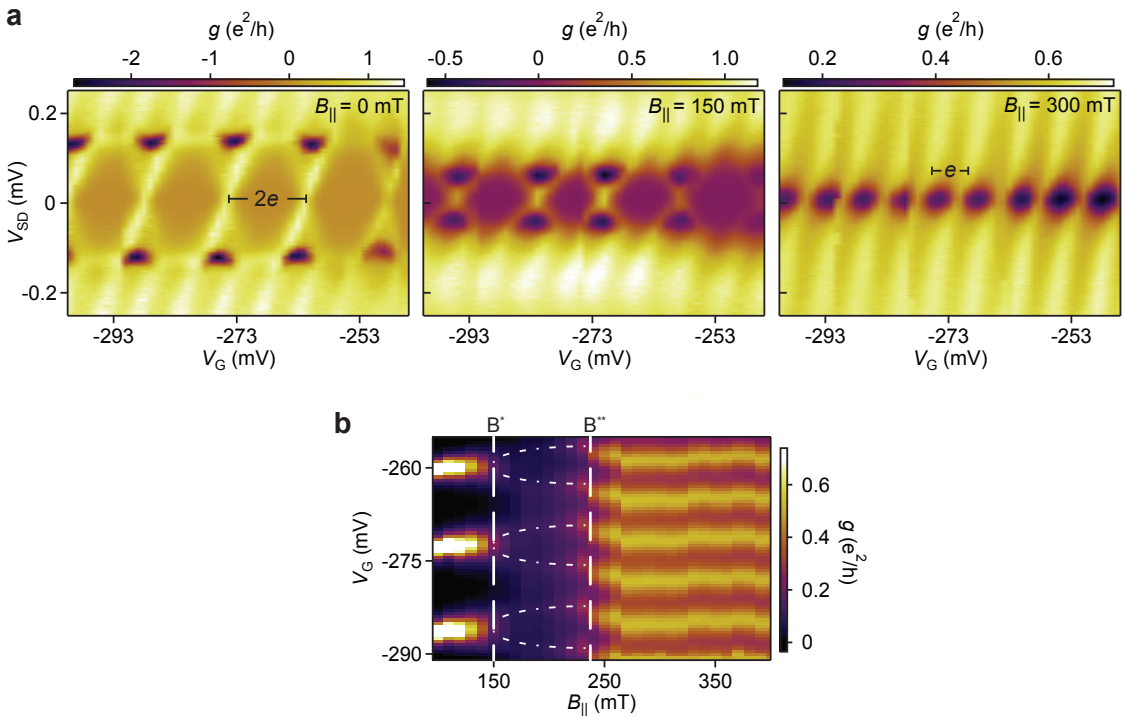

Figure 5.8: Coulomb diamonds in a magnetic field.**a**) Differential conductance g as a function V_{SD} and V_G at parallel magnetic fields of $B_{\parallel} = 0$, 150 and 300 mT. At $B_{\parallel} = 0$ the Coulomb diamonds are evenly spaced. At $B_{\parallel} = 150$ mT the odd-charge state is energitcally lowered and beginning to broaden the Coulomb diamonds. At $B_{\parallel} = 300$ mT, the Coulomb diamonds are again evenly spaced at half the distance compared to $B_{\parallel} = 0$. This indicates a transition from $2e$ Cooper pair tunneling to $1e$ quasiparticle tunneling as indication of the formation of a Majorana zero mode. **b**) Differential conductance g as a function V_G and $B_{\parallel}$ shows Coulomb peaks measured at $V_{SD} = 0$ transition from a $2e$ charge periodicity to a $1e$ periodicity. The transition starts at $B^* = 150$ mT and ends at $B^{**} = 230$ mT. The conductance intensity at between B^* and B^{**} drops considerably and regains intensity. This is an indication of Majorana teleportation.[21]

negative differential conductance is decreased. At B = 300 mT, well below the critical field B_C[i], the distance between Coulomb resonances within and above the superconducting gap are the same. This indicates a finished transition from a $2e$ periodicity to a $1e$. As discussed, and also recently observed in proximitized InAs nanowires by Albrecht et al., this is caused by the lowering of the odd charge state

[i] As measured in the tunneling device. As seen in fig.5.5.

by the Zeeman energy as explained in section 2.2.2.[14].

As seen in fig. 5.8 **b** differential conductance as a function of V_G at $V_{SD} = 0$ shows Coulomb resonances evolved in a parallel magnetic field, $B_{\parallel}$. A $2e$ peak spacing is seen until $B^* = 150$ mT. Between B^* and B^{**} a noticeable drop in intensity is observed, before the full transition from $2e$ to $1e$ is completed. This transformation of the Coulomb peaks at $V_{SD} = 0$ in a parallel magnetic field is in good agreement with theory on Majorana teleportation.[19;20]

Conclusion and Outlook 6

The work is rounded off by a summary of its most prominent findings followed by an outlook discussing natural follow-up experiments and broader perspective "next-steps".

6.1 Conclusion

The presented work provides 3 different electrical studies on InAsSb nanowires:

First, weak antilocalization measurements are performed on individual segments of $InAs_{1-x}Sb_x$ nanowires with a stepped change in Sb molar fraction. From fits to the weak antilocalization traces of the individual nanowire segments the spin-orbit length and Rashba spin-orbit coefficient is plotted as function of Sb concentration. These measurements are compared to a theoretical proposal predicting high spin-orbit interaction in alloyed InAsSb nanowires around Sb molar fractions of ~ 0.6. The same qualitative trend is verified experimentally. Additionally, it is discussed how the band structure of InAsSb nanowires could provide increased spin-orbit interaction. A spin-orbit length $l_{SO} = 35$ nm for $InAs_{0.52}Sb_{0.48}$ nanowires is found - the lowest reported, so far. This indicates a high spin-orbit interaction in alloyed InAsSb nanowires.

Second, tunneling experiments are conducted on $InAs_{0.2}Sb_{0.8}$ nanowires with epitaxially grown Al on 2 facets. These show proximitized superconductivity with a hard superconducting gap of $\Delta = 230$ μeV. From Yu-Shiba-Rusinov states and Andreev bound states Landé g-factors of the order of 6-17 are extracted. From an extrapolated Rashba coefficient, measured g-factors and the induced superconducting gap a topological phase transition is estimated to occur at $B_{\parallel} \sim$ 0.23-0.7 T. This is indeed verified by evolving pairs of Andreev bound states in a parallel magnetic field where Majorana zero modes form at $B_{\parallel} = 0.3$ T and $B_{\parallel} =$ 0.38 T. This is the first report on Majorana zero modes in InAsSb nanowires using tunneling spectroscopy.

Third, Coulomb spectroscopy is performed on the same $InAs_{0.2}Sb_{0.8}$ nanowires with 2 facet Al showing Coulomb oscillations with a $2e$ periodicity at a source-drain bias $V_{SD} = 0$. When the Coulomb oscillations are evolved in a parallel magnetic field a transition from $2e$ to $1e$ periodicity is observed. The transition finishes at $B^{**} = 230$ mT which corresponds to the estimated magnitude of a topological phase transition in $InAs_{0.2}Sb_{0.8}$ nanowires. This is evidence of Majorana zero modes residing at the ends of the proximitized island. Additionally, an intensity drop during the $2e \rightarrow 1e$ transition is observed which could be correlated to Majorana teleportation. This is the first report on signatures of Majorana zero modes in InAsSb nanowires using Coulomb spectroscopy.

As a last comment it should be stated that $InAs_{1-x}Sb_x$ nanowires could provide an excellent platform for transitioning into the topological regime and thus hosting Majorana zero modes. Its ternary structure allows for control of the spin-orbit interaction in the nanowires based on the Sb/As ratio, which is a parameter that cannot be controlled in binary InAs or InSb nanowires. These are nanowire platforms that so-far have provided signatures of Majorana zero modes.[14;13;53;54]

6.2 Outlook

Growing $InAs_{1-x}Sb_x$ with an Sb molar fraction in the full range of x = 0 to 1, would be highly desirable in order to obtain a full picture of the spin-orbit interaction in InAsSb nanowires. Most likely, proximitized $InAs_{0.4-0.6}Sb_{0.6-0.4}$

nanowires would yield larger spin-orbit splitting of the conduction band and result in a more protected Majorana zero mode.[10] Additionally growing a thinner Al shell on the InAsSb nanowires, could improve on critical magnetic fields, B_C^{Al}.[55] Exploring different superconducting materials with critical fields larger than B_C^{Al}, such as Nb and V, could also yield a bigger magnetic field parameter space.

As described in section 1 the non-Abelian exchange statistics of the Majorana zero modes have to be shown in order to definitely verify whether or not Majorana zero modes behave as Majorana fermions. This could be performed in braiding experiments as already theoretically proposed in nanowire networks.[56]

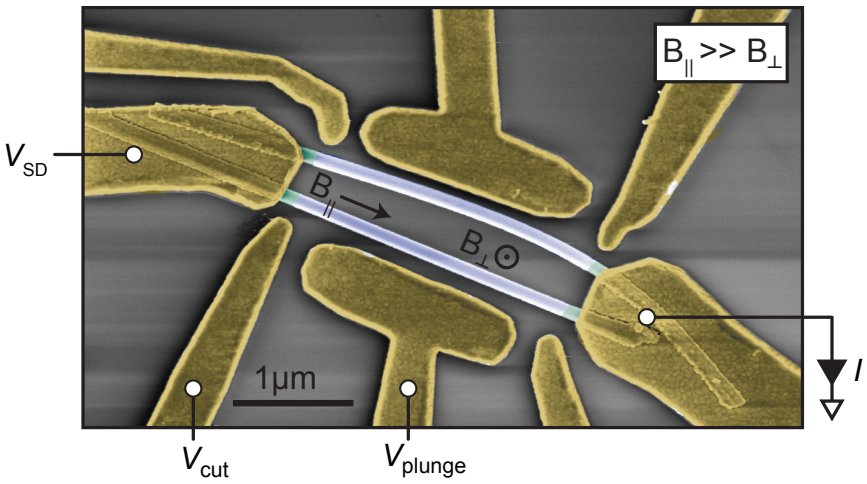

FIGURE 6.1: Majorana Interferometer device. Two NISIN nanowire geometries shorted by the same Ti/Au leads enclosed an area of which a flux can be threaded through. Image courtesy Aske Gejl.

Since parallel magnetic fields are crucial for the emergence of Majorana zero modes, establishing these in larger networks of nanowires could prove hard - however, a theoretical proposal of a Majorana interferometer would allow the detection of non-Abelian exchange statistics, without the introduction of braiding schemes. This technique could detect the non-Abelian nature of Majorana zero modes disregarding fast gates and read-out techniques, and still operate in parallel magnetic fields.[57] Preliminary experiments were initiated on just these interferometers through-out the last part of this thesis. A false coloured scanning electron micrograph of a

measured interferometer device consisting of two InAs nanowires with epitaxial Al on two facets is seen in fig. 6.1

Appendix 7

7.1 Device Fabrication

This sections concerns itself with the fabrication process of the different approaches to device construction that this thesis will entail. There will be distinguished between fabrication of side gated, top gated and bottom gated devices. Since a lot of the same principles, e.g. electron beam lithography etc., are the same for all different gating techniques, these will only be discussed in the first section. It should be mentioned that these fabrication techniques can readily be redesigned to accommodate for other needs like fabrication of bonding pads (which was indeed the case), and also where this section will start.

7.1.1 General cleaning

A clean chip is paramount, since dust and small fibers are on a much greater scale than the devices you will want to be making. The general cleaning procedure involves:

- Sonicating in Acetone for 2 min.
- Sonicating in Isopropanol for 2 min.

- Rinse thoroughly in Mili-Q.
- O_2 plasma ash for 1 min.

7.1.2 Depositing nanowires

The two different nanowire deposition techniques used in this thesis now follow in no particular order[i]:

- Dry transfer technique #1: *using a clean-room wipe*
- Dry transfer technique #2: *using a micromanipulator*

Only two deposition technique were used for the devices discussed here, namely the so-called *clean-room wipe* technique, and the micromanipulator technique. The clean-room wipe technique is not always the least wasteful, nor the cleanest[ii] - but definitely the quickest. It has been by far the most used technique for this work because it allows one to quickly fabricate a large number of devices if you do not care about the placement of one nanowire with respect to another. For some device geometries the micromanipulator technique has proved invaluable. It is extremely economical[iii] and precise, but it does consume your time, even with practice.

Clean-room wipe technique

Cut out an acute triangle of a piece of clean room wipe with roughly the same size and shape as shown in fig. 7.1. Note that cutting alongside the fibers of the clean-room wipe ensures that the tip does not fray to easily[iv], making you pick up too many wires and potentially contaminating your chip with large fibers.

Hereafter the tip of the acute triangle is bent 90° making sure that you can actually see what you are doing from your own hand. Next, the recently cleaned set of bonding pads is placed next to the growth chip. The very tip of the clean-room

[i] Other nanowire deposition techniques exist and will be colloquially called "the wet transfer technique" and the "growth wafer chip".

[ii] But with practice it becomes reasonably clean and nanowire economical

[iii] Imagine only picking up one nanowire from a growth chip with a few billion nanowires per device you want to build. You'll most likely change your career before going through the whole growth wafer.

[iv] Thank you Willy Chang for that one!

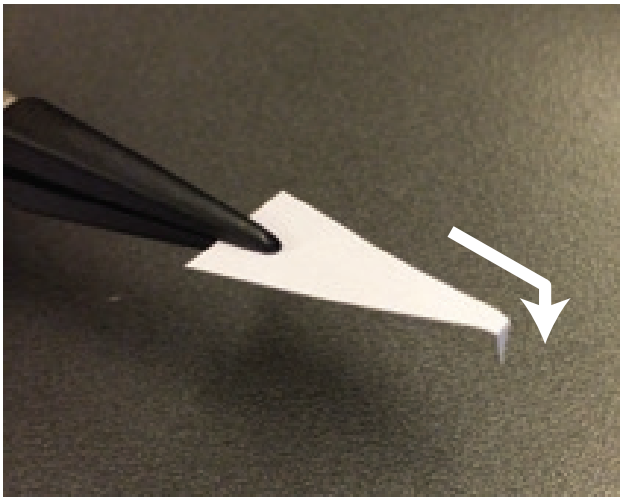

FIGURE 7.1: Tip of a tweezer holding clean-room wipe bent in order to easily deposit nanowires.

wipe is now **extremely** *gently* dabbed on a random (or not random) part of the growth wafer. No swiping should be needed, only the very tip should touch the wafer and pick up a "few" nanowires. With the same delicacy the tip of the clean room wipe is dabbed on in the center of the bonding pad releasing nanowires onto your substrate via van der Waals interaction. The chip is now investigated in an optical microscope to check if the number of deposited wires is satisfactory. Repeat if necessary.

Micromanipultar technique

The micromanipulator technique involves picking up one select nanowire at a time. The micromanipulator station is basically composed of a needle with a diameter of between $\emptyset = 0.1\mu m - 0.25\mu m$ connected to an actual micromanipulator station and an optical microscope. The growth substrate and a set of bonding pads are placed on a motorized stage. Starting at the lowest magnification on the optical microscope and the needle at a z-position with sufficient spacing between the growth substrate and the tip, the tip of needle is centered and focus is found. Gradually lowering the focus and change the z-height and keeping the focal point on the nanowire tip ensures that the small needle is not dissappearing out of

view-field and focus, in an iterative manner. At certain points during this process one wants to switch to higher magnification in order to actually see the nanowires. This process is continued iteratively until the substrate becomes apparent and with caution the nanowire tip is lowered without smashing it onto the nanowires. If that happens, one must restart the process with a new needle because the needle will now be covered in a thick layer of nanowires and substrate[v]. Trying to deposit nanowires from a contaminated needle result only in the transfer of broken wires and dirt. The situation one wants to end up in is the top of the forest of nanowires in focus and the needle positioned slightly higher and out of focus. Now browsing for suitably positioned nanowires begins. Low density growth wafers are the easiest to work with, simply because accessing a single nanowire is straightforward. The basic principles using the micromanipulator is sketched in fig. 7.2. For high density wafers with positioned nanowires finding the corner of the array and picking up the corner-most nanowire is the easiest. Randomly distributed wires in high density are trickier, here two approaches are fitting. (1) Search around on the whole of the growth wafer for lower densities. The temperature gradient across the growth wafer during growth will typically yield different densities. (2) Clear out a nanowire forest to controllably access a distinct nanowire[vi].

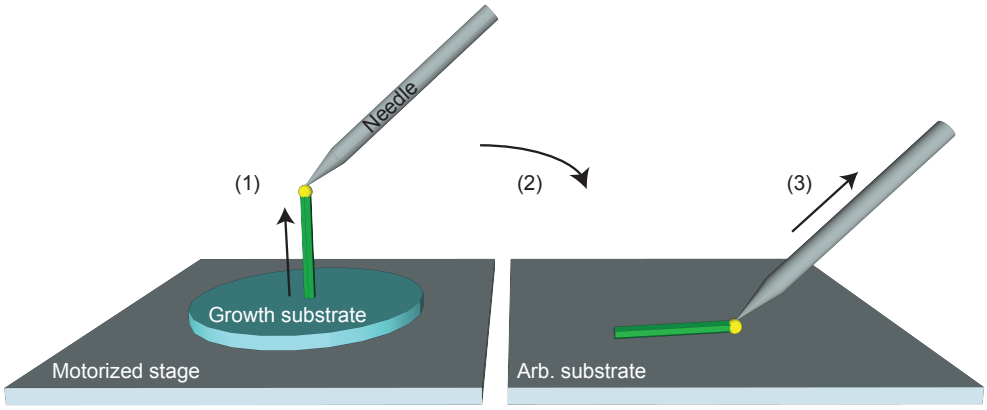

Figure 7.2: Three steps of the micro-manipulator nanowire transfer technique.

[v] And yes, it happens.
[vi] This would typically be the case when trying to pick up merged nanowires.

7.1.3 Side gates and contacts

This section will entail what seems like two different sections in one, namely fabrication of sidegates and contacts to the nanowire - the reasoning is simple: they are made simultaneously. The following section will cover the principles of electron beam lithography (EBL) specifically for nanowires.

7.1.3.1 Electron beam lithography

Here the steps of electron beam lithography will be explained and discussed.

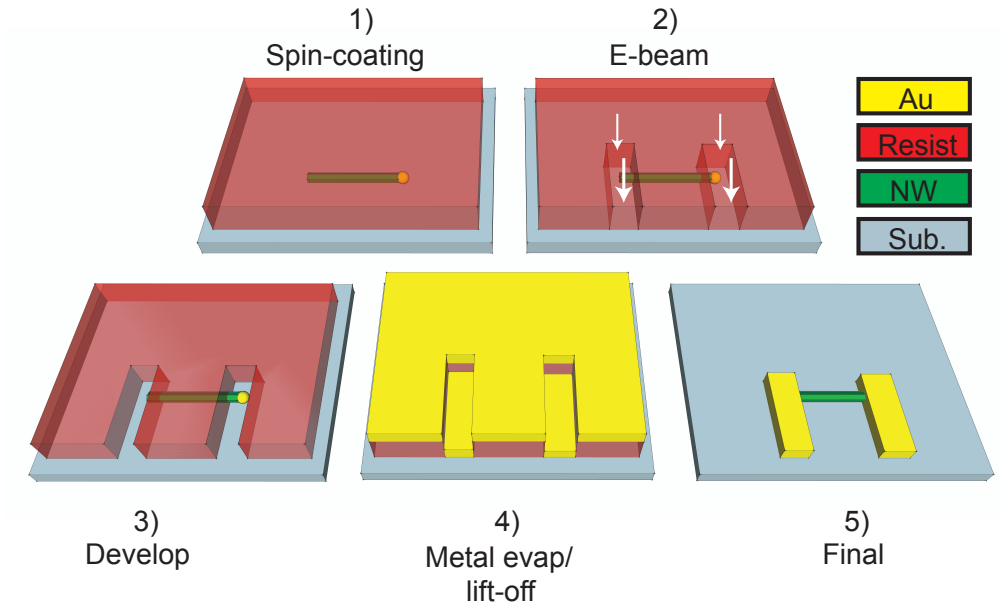

FIGURE 7.3: The principles of electron beam lithography. The steps are: 1) Spin-coat a electron beam sensitive polymer on the chip already covered in nanowires. 2) Expose desired regions of the polymer to doses of electrons in order to break the polymeric chains to make the certain parts of the polymer susceptible to a developing solution. 3) Develop the exposed parts of the polymer. 4) Deposit a metal (in this case Au is used) onto the whole chip, and let the chip sit in a solvent to lift-off all remaining resist. 5) The final device is ready with Au only covering the areas exposed to the electron beam.

1) Spin coating

Resist consists of a photo or electron-beam sensitive polymer diluted in a solvent.

Depending on desired resolution and yield specifications, one would choose e-beam resist because the wavelength of electron is considerably smaller compared to infrared light which would be used for photo-sensitive resist, as opposed to photo-resists which by means of a mask (or a LASER) can produce large arrays of repeating patterns in a matter of seconds. This work only used e-beam resist because of the demand for chip-to-chip designability and very high resolution.

The deposited nanowires have a distinct diameter which has to be accounted for when choosing the resist and to which degree it is diluted. The degree of dilution determines the height of the polymer alongside the acceleration, rotations per minute and the spin time chosen on the spinner. A spin-chart found from the resist-dealer will guide one to a great place to start. The resist used in this work is from MicroChem and is a PMMA. Based on the diameter of $\sim$ 80-100 nm of the used nanowires, the resists used in this work is either a single layer of A6 or double layer A4, which both can be found in fig. 7.4.

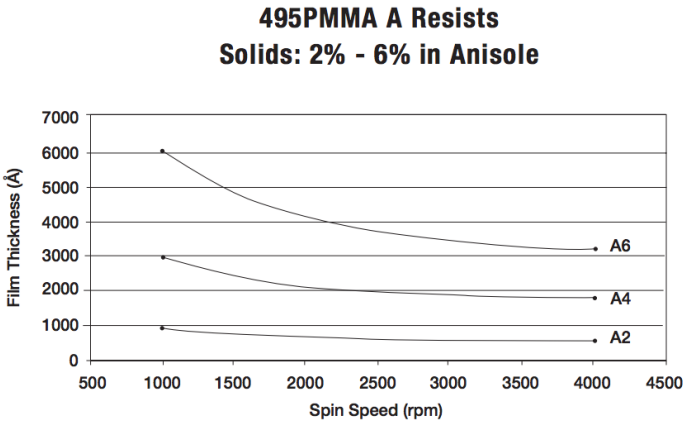

Figure 7.4: The applied spin chart from Micro-Chem.

The generic recipe for one layer of resist is as follows[vii]:

- #1 Rinse chip by sonicating in acetone for 2 min and in isopropanol for 2 min and blow dry with nitrogen.
- #2 Ash in oxygen plasma asher for 45-60 sec. to remove any organic residue

[vii] For double layers simply repeat the recipe

- #3 Place the chip on the vacuum chuck in the spinner. Let it accelerate up to 500 rpm and pause the program, while the sample is still spinning drop $\sim 8\mu L$ of A6 onto the chip of size $\sim 4 \times 4$ mm and start the program again. The program chosen spins the sample at 4000rpm for 60 sec.
- #4 Bake the sample at 185°C for 2 min.

After baking the solvent has evaporated and the polymeric chains are cross-linked and hardened.

2) E-beam

In a design software[viii] the desired pattern is drawn and exported to Beamer which is a proximity effect correction program. Based on acceleration voltage, resist type, substrate type and design density Beamer accounts for secondary and backscattered electrons. Beamer breaks the design into small segments and corrects individual doses for each section and adjusts the number of electron shots for each segment. This ensures that high density patterns are not overexposed and low density patterns are not underexposed - this step is crucial for reproducibly making high density and extremely thin bottom gates which will be discussed in sec. **??**. Next, the sample is loaded into the Elionix ELS-7000 which is a 100keV SEM with a patterning processor that exposes the recently made design onto the chip making the exposed parts of the resist sensitive to the developer solution.

The specifications chosen are:

- #1 600 μm writefield size
- #2 500 pA dose
- #3 240 000 dots per writefield
- #4 0.14 μ sec/dot

3) Develop

Developing involves submersing and swirling the exposed chip in 1:3 diluted methyl isobutyl ketone/isopropanol (MIBK/IPA) for 60 s and rinsing in pure IPA for roughly 30 s. This process will remove only the exposed resist and leave the non-exposed resist intact.

4) Metal evaporation and lift-off

Organic residue in the developed regions is removed by ashing the sample in a oxygen plasma asher for 45 s before loading the sample in a e-beam evaporation chamber. In case of this study the sample is loaded into a combined 10kV AJA

[viii] Many softwares do the same trick with little difference. To mention a few: AUTOCad, Clewin and DesignCAD.

metal evaporation, sputtering and ion milling system operating at $\sim 10^{-8}$ Torr. First step now is to remove the native oxide on the nanowire. The chamber with sample is flooded with Ar and ignited creating a plasma. Hereafter a microwave frequency at a power of 50W is used to oscillate the Ar ions for 4 min and 20 s i.e. removing the oxide layer on the semiconductor. Hereafter 5 nm of Ti is used as a sticking layer before evaporating 120 nm of Au. After unloading the sample, it is placed in a beaker with a closed lid for $\sim 1h$ heated to 60°C. Next, a small 10mL plastic pipette is dunked in the still hot acetone and used to jet off the Au on the resist - leaving only the pattern drawn in the design software defined in Ti/Au.

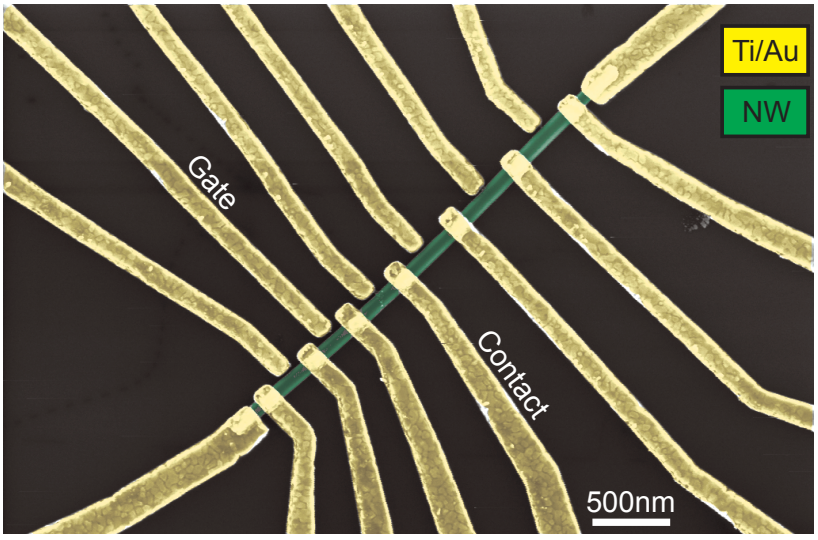

FIGURE 7.5: False-coloured scanning electron micrograph of a final device measured in this thesis.

5) Final

If the lift-off process turned out is successful the outcome of one of the devices used in this study is presented as seen on the false-coloured SEM image in fig. 7.5. The Au leads that do not touch the nanowire are called gates whereas the other Au leads are called the contacts. Contacts are used to make electrical contact to the semiconductor whereas gates can change the electrostatic potential landscape. This device will be explained in greater detail later.

7.1.4 Bottom gates

Since side gates have limited strength and the gating ability is dependent on the distance between between the semiconductor and the gate, bringing the gates even closer to the nanowire might greatly improve the gateability. However, E-beam lithography has its precision limitations and might short to the nanowire instead of only reaction electrostatically with the nanowire. A great alternative to sidegates is bottom gates. Bottom gating relies on fabrication of Au electrodes as a first, covering them by a dielectric, depositing the nanowires on the dielectric and later selecting the desired bottom gates in the same lithography step as when making contact to the deposited nanowire. Bottom gates have great advantages, it requires little precision when placing the nanowires and all gates are as close to the nanowire as the thickness of the dielectric. See fig. 7.6**a,b** for before and after ALD of HfO_2 on bottom electrodes SEM images with the provided specifications in the recipe.

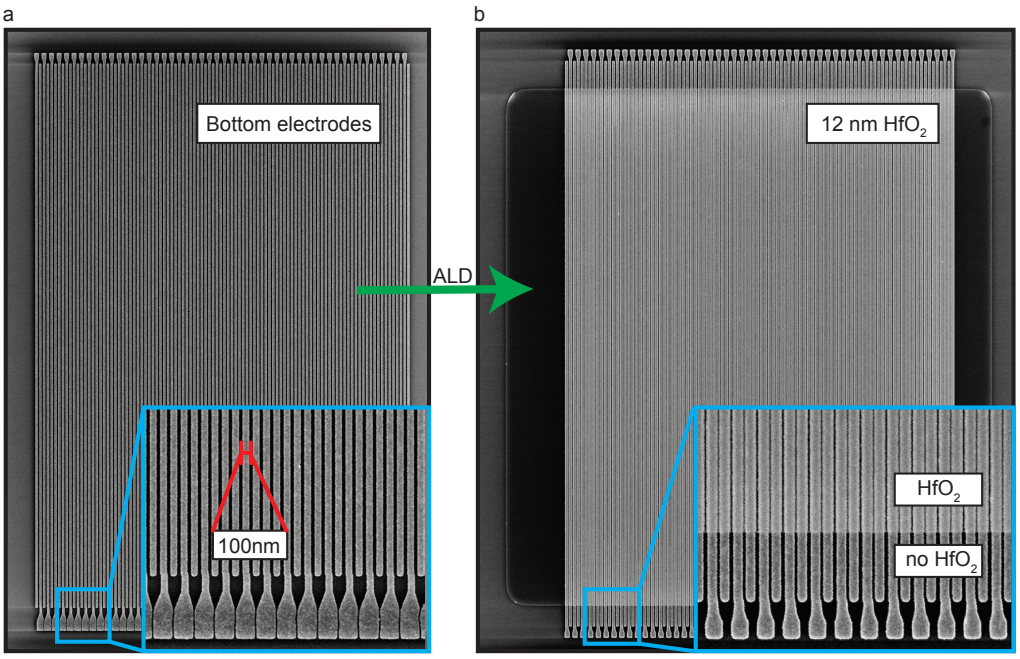

Figure 7.6: The principles of bottom-gate fabrication. **a**) EBL defined bottom gate electrodes. **b**) The bottom gate electrodes covered by 12 nm HfO_x. The electrodes are uncovered in top and bottom to allow for access to individual electrodes.

The recipe is as follows:

- #1 Spin a single thin layer of resist. A2 or A4.
- #2 Design desired bottom-gate pattern and expose as previously described[ix].
- #3 Develop as previously described.
- #4 Deposit 25-30 nm of Au and lift-off as previously described.
- #5 Spin double layer of resist. A thick co-polymer like EL9 and a regular PMMA like A6.
- #6 Expose, preferably rounded resist windows[x], the desired part of the bottom electrodes that is supposed to be covered in dielectric.
- #7 Develop and ash as previously described.
- #8 Atomic layer deposit desired thickness of HfO_2.
- #7 Lift-off as previously described with the added step of sonicating at high amplitude and low frequency. This will knock over the ALD sidewalls.

7.1.5 Al etching

For the Majorana fermion devices presented later, a crucial step is the tailoring of the exact patterns of the epitaxially grown Al on the nanowires. Following the the E-beam steps until and including step 3) Develop, as discussed earlier, resist windows are defined via E-beam lithography. This provides the necessary control over where the etching of the epitaxial Al is desired.

The following recipe is utilized:

- #1 In a beaker with closed lid heat Al etch transene D in a heat-bath to 55 °C and let sit for 15 min, to stabilize temperature. Copy the same principle

[ix] The spacing and thickness of these bottom gates are conservatively chosen, such that the standard e-beam lithography settings can be applied. 100 nm wide bottom-gates are absolutely fine for most situations.

[x] The lack of corners will later aid you knock down the dielectric walls that are built up during the ALD.

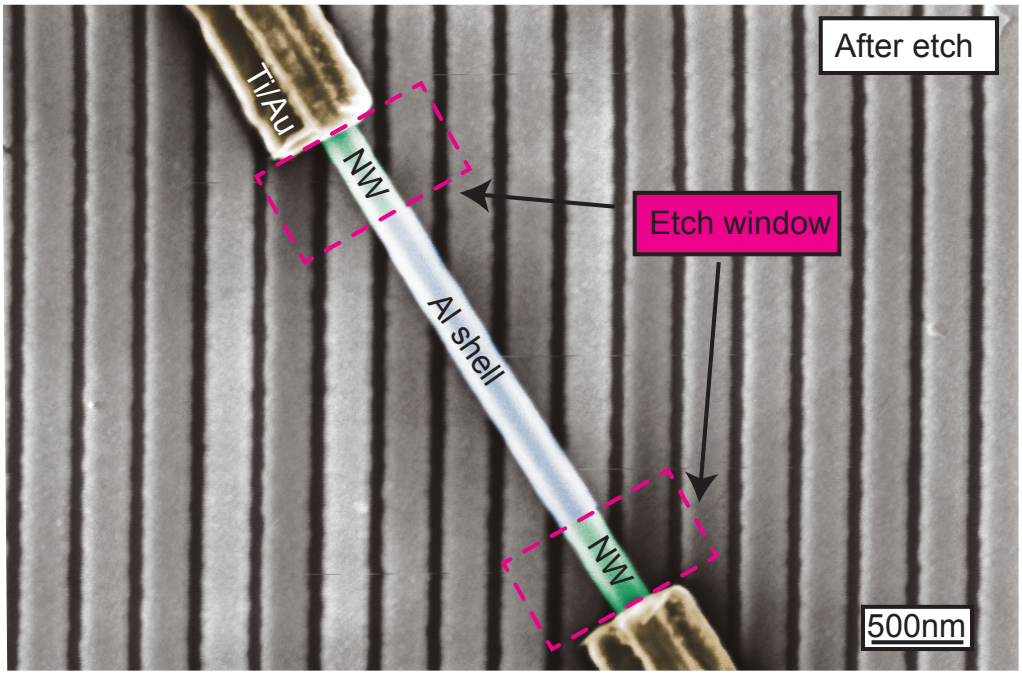

Figure 7.7: Selectively removing Al off of nanowires. A nanowire with Al grown on 2 facets is contacted by EBL. Defining etching mesa in resist by repeating the EBL procedures from 1 to 3, the nanowires is held in Al etchant type D for 10 sec. and thoroughly rinsed in Mili-Q water. This results in selectively removed Al off the nanowire.

only with Mili-Q water and an open beaker. This allows you to continually measure the temperature of the Mili-Q water giving you a clear indication of the temperature of the highly corrosive etchant.

- #2 Dunk the chip covered with resist in the heated etchant and swirl for 10 s.
- #3 Clean in 3 beakers of Mili-Q. A few seconds in the first, and 30 s in the remaining two.
- #4 Clean in IPA for 30 s.

See fig. 7.7 for an SEM image after the described etching procedure and after the resist has been stripped in acetone at 60°C for 10 min and ashed for 45 s.

7.1.6 Top gates

Top gates are typically more effective than side gates based on the same argument presented in the bottom gate section. When bottom gates are times consuming and sometimes difficult to fabricate a new and quicker way of fabricating top gates can be applied.

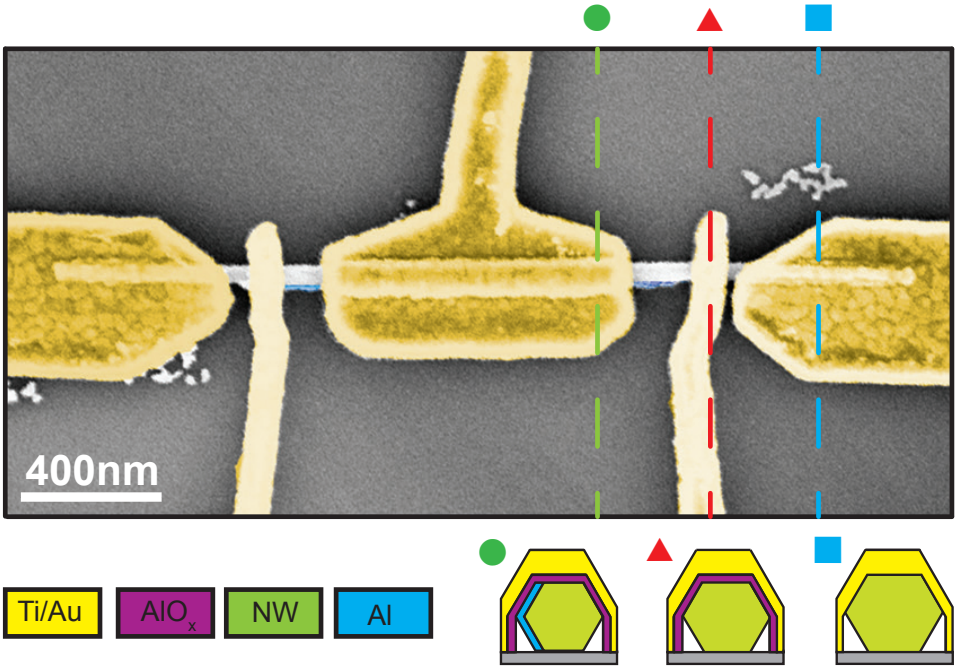

FIGURE 7.8: False-coloured scanning electron micrograph of the top-gated *Copenhagen* device. Yellow, Ti/Au contacts; green, $InAs_{0.2}Sb_{0.8}$ nanowire; blue, two-facet Al; purple, AlO_x. V_{SD}, applied bias voltage; I, measured current; V_G, gate voltage. Three differently colored line-cuts show three cross-sections of the device structure. Green circle is the structure of the Ti/Au top-gate isolated from the nanowire with an Al shell by AlO_x. Red triangle is the structure of the Ti/Au top-gate isolated from the nanowire by AlO_x. Blue square is Ti/Au contacts to the nanowire. Inset: Schematic illustration of the *Copenhagen* geometry.

This approach to making top gates requires two lithography steps, which is the same number of steps as for bottom gates. However, no lengthy ALD process is necessary, which will save you at least 12h, because fancy trick involving AlO_x is applied. See fig. 7.8 for false-coloured SEM image of one the devices based on

this principle. The three cross-section cartoons illustrate the layering sequence of Ti/Au, AlO_x and Al of the different parts of the nanowire. Ohmic contacts are made to the ends of the nanowire. The two cutter and the plunger gates are isolated from the nanowire by roughly 10-15nm of AlO_x. This dielectric is constructed by repeatedly depositing a very thin film of Al and subjecting the film to atmospheric air in order to oxidize the Al building the insulator, in a less time consuming way than what ALD typically requires. It should however be noted that this system is assumed to host charge traps that could give rise to unstable gate performance. These effects were not studied.

Assuming that contacts and etching steps are already performed, the recipe is as follows:

- #1 Spin resist, a standard double layer A4 will suffice.
- #2 Via EBL define the top-gates in the resist.
- #3 Develop as previously described.
- #4 Instead of regular RF ion milling, deposit 1-2 nm of Al onto the sample. Unload the sample at let it sit at athmospheric air for 5 min. This will oxidize the Al into AlO_x which is a dielectric with reasonably high dielectric constant κ.
- #5 Repeat step #4 five times.
- #6 Deposit 5nm of Ti and 120nm of Au as previously described.
- #7 Lift-off as previously described.

7.2 Landé g-Factors

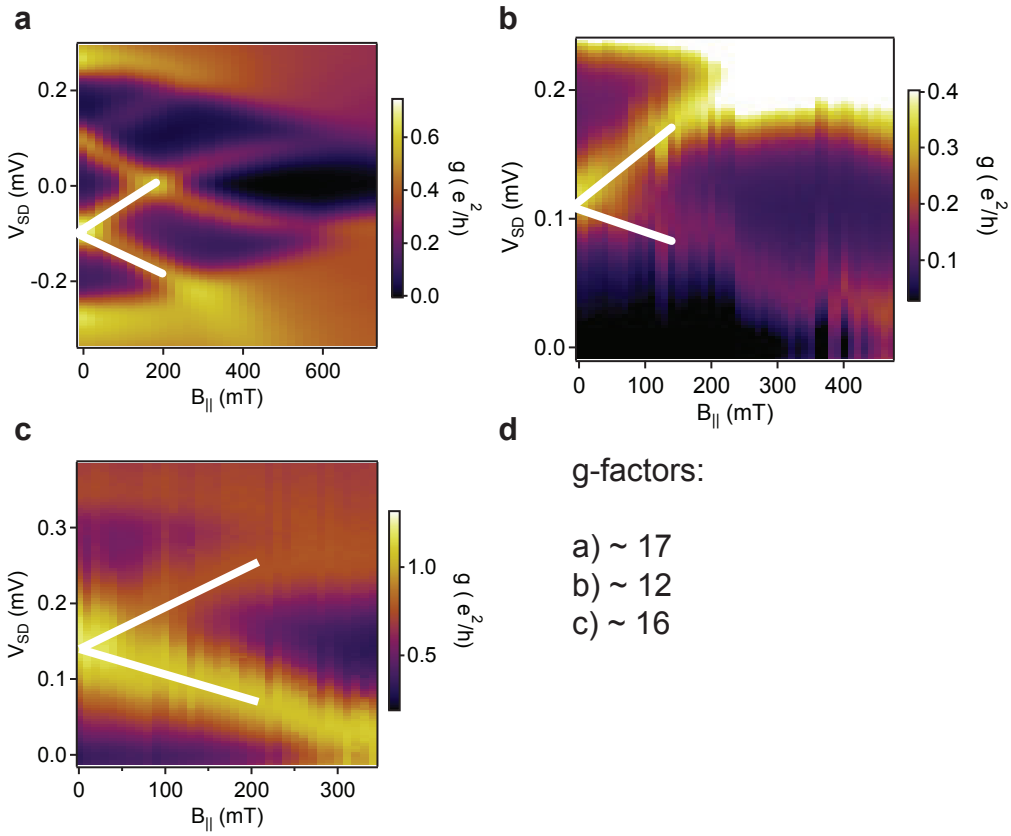

FIGURE 7.9: Additional g-factors. **a-c**) Differential conductance, g, as a function of source-drain bias, V_{SD}, and parallel magnetic field $B_{||}$. White lines indicate the g-factor. **d**) Table of corresponding g-factors.

7.3 List of Chips

List of Chips:

Spin-orbit Chips

Side-gated devices

#1. SbGradientDevI: NWs are called “Thomas Dots”, EBL fail

#2. SbGradientDevII: NWs are called “Thomas Dots”, EBL fail

#3. SbGradientDevIII: NWs are called “Thomas Dots”, EBL succesful, interesting SOI data

Majorana Chips

Side-gated devices

#1. Orangutang1: Qdev310 NWs, testing contacts

#2. Orangutang2: Qdev310 NWs, testing CPH & Delft devices +etch test

#3. Orangutang3: Qdev310 NWs, testing CPH & Delft devices. Likely fridge issues

Top-gated devices

#1. Honeybadger 1: Qdev253 NWs, etched too long

#2. Honeybadger 2: Qdev310 NWs, CPH shows MZMs

Bottom-gated devices

#1. Honeybadger 3.1: Qdev310 NWs, bottom gates tested

#2. Honeybadger 3.2: Qdev310 NWs, Delft geo shows MZMs

Figure 7.10: List of chips relevant to the thesis.

7.4 Universal conductance fluctuations and Averaging Amplitudes

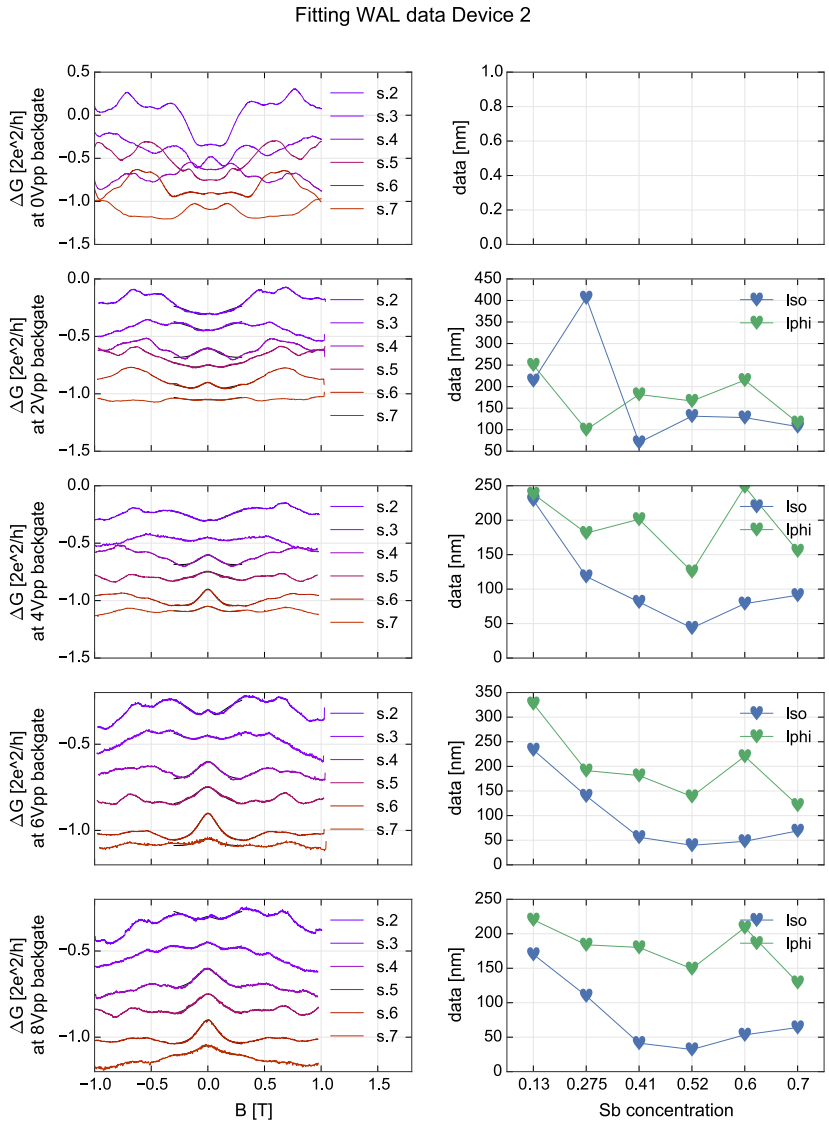

FIGURE 7.11: Weak antilocalization fitting as a function of gate averaging. As seen UCF averaging is necessary to resolve weak-antilocalization features. Already at $V_{pp} = 2V$ the trend in l_{SO} as a function of Sb concentration is clear. Quantitative Sb concentrations have been modified later for accuracy.

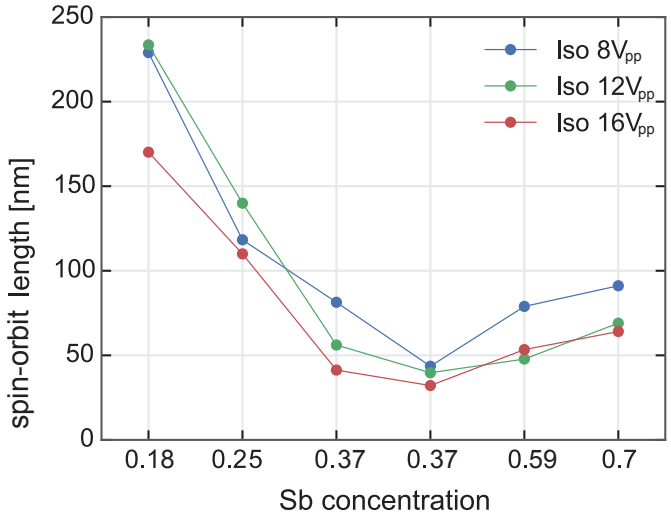

Figure 7.12: UCF averaging amplitudes and spin-orbit length. For different amplitudes of, V_{pp}, no noticeable difference in spin-orbit length l_{SO} is evident.

Bibliography

[1] G. E. Moore, "Lithography and the future of moore's law," in *SPIE's 1995 Symposium on Microlithography*, pp. 2–17, International Society for Optics and Photonics, 1995.

[2] P. Clarke, "More varied research needed beyond 10-nm, says intel." Available online at $http://www.eetimes.com/document.asp?doc_id = 1263255$.

[3] U. Pirzada, "Intel isscc: 14nm all figured out, 10nm is on track, moores law still alive and kicking." Available online at http://wccftech.com/intel-isscc-14nm/.

[4] R. P. Feynman, "Quantum mechanical computers," *Foundations of physics*, vol. 16, no. 6, pp. 507–531, 1986.

[5] D. P. DiVincenzo, "Topics in quantum computers," in *Mesoscopic electron transport*, pp. 657–677, Springer, 1997.

[6] M. Freedman, A. Kitaev, M. Larsen, and Z. Wang, "Topological quantum computation," *Bulletin of the American Mathematical Society*, vol. 40, no. 1, pp. 31–38, 2003.

[7] A. Stern, "Non-abelian states of matter," *Nature*, vol. 464, no. 7286, pp. 187–193, 2010.

[8] A. Stern and N. H. Lindner, "Topological quantum computationâĂŤfrom basic concepts to first experiments," *Science*, vol. 339, no. 6124, pp. 1179–1184, 2013.

[9] A. Y. Kitaev, "Fault-tolerant quantum computation by anyons," *Annals of Physics*, vol. 303, no. 1, pp. 2–30, 2003.

[10] Y. Oreg, G. Refael, and F. von Oppen, "Helical liquids and majorana bound states in quantum wires," *Physical review letters*, vol. 105, no. 17, p. 177002, 2010.

[11] M. Leijnse and K. Flensberg, "Introduction to topological superconductivity and majorana fermions," *Semiconductor Science and Technology*, vol. 27, no. 12, p. 124003, 2012.

[12] E. Majorana, "Teoria simmetrica dellâĂŹelettrone e del positrone," *Il Nuovo Cimento (1924-1942)*, vol. 14, no. 4, pp. 171–184, 1937.

[13] V. Mourik, K. Zuo, S. M. Frolov, S. Plissard, E. Bakkers, and L. Kouwenhoven, "Signatures of majorana fermions in hybrid superconductor-semiconductor nanowire devices," *Science*, vol. 336, no. 6084, pp. 1003–1007, 2012.

[14] S. Albrecht, A. Higginbotham, M. Madsen, F. Kuemmeth, T. Jespersen, J. Nygård, P. Krogstrup, and C. Marcus, "Exponential protection of zero modes in majorana islands," *Nature*, vol. 531, no. 7593, pp. 206–209, 2016.

[15] M. Tinkham, *Introduction to superconductivity*. Courier Corporation, 1996.

[16] C. Timm, "Theory of superconductivity." Available online at `https://www.physik.tu-dresden.de/~timm/personal/teaching/thsup_w11/Theory_of_Superconductivity.pdf`, 2011.

[17] D. Chevallier, P. Simon, and C. Bena, "From andreev bound states to majorana fermions in topological wires on superconducting substrates: A story of mutation," *Physical Review B*, vol. 88, no. 16, p. 165401, 2013.

[18] J. Hergenrother, M. Tuominen, and M. Tinkham, "Charge transport by andreev reflection through a mesoscopic superconducting island," *Physical review letters*, vol. 72, no. 11, p. 1742, 1994.

[19] L. Fu, "Electron teleportation via majorana bound states in a mesoscopic superconductor," *Physical review letters*, vol. 104, no. 5, p. 056402, 2010.

[20] R. Hützen, A. Zazunov, B. Braunecker, A. L. Yeyati, and R. Egger, "Majorana single-charge transistor," *Physical review letters*, vol. 109, no. 16, p. 166403, 2012.

[21] D. Liang and X. P. Gao, "Strong tuning of rashba spin–orbit interaction in single inas nanowires," *Nano letters*, vol. 12, no. 6, pp. 3263–3267, 2012.

[22] T. Ihn, *Semiconductor Nanostructures: Quantum states and electronic transport*. Oxford University Press, 2010.

[23] I. Van Weperen, *Quantum Transport in Indium Antimonide Nanowires: Investigating building blocks for Majorana devices*. TU Delft, Delft University of Technology, 2014.

[24] S. Chakravarty and A. Schmid, "Weak localization: The quasiclassical theory of electrons in a random potential," *Physics Reports*, vol. 140, no. 4, pp. 193–236, 1986.

[25] M. Kozicki and M. Mitkova, "Nanotechnology: Volume 3: Information technology," 2008.

[26] C. Beenakker and H. Van Houten, "Boundary scattering and weak localization of electrons in a magnetic field," *Physical Review B*, vol. 38, no. 5, p. 3232, 1988.

[27] G. Batey, Graham. Teleberg, "Principles of dilution refrigeration." Available online at $http://www.oxford-instruments.cn/OxfordInstruments/media/nanoscience/Priciples-of-dilution-refrigeration_v14.pdf$.

[28] F. Pobell, *Matter and methods at low temperatures*. Springer Science & Business Media, 2007.

[29] V. W. Chin and T. Tansley, "Alloy scattering and lattice strain effects on the electron mobility in in 1- x ga x as," *Solid-state electronics*, vol. 34, no. 10, pp. 1055–1063, 1991.

[30] T. Katoda, F. Osaka, and T. Sugano, "Electron mobility in in1-xgaxas epitaxial layer," *Japanese Journal of Applied Physics*, vol. 13, no. 3, p. 561, 1974.

[31] T. Ando, "Self-consistent results for a gaas/al x ga1-x as heterojunciton. ii. low temperature mobility," *Journal of the Physical Society of Japan*, vol. 51, no. 12, pp. 3900–3907, 1982.

[32] L. R. Weisberg, "Anomalous mobility effects in some semiconductors and insulators," *Journal of Applied Physics*, vol. 33, no. 5, pp. 1817–1821, 1962.

[33] G. Petersen, S. E. Hernández, R. Calarco, N. Demarina, and T. Schäpers, "Spin-orbit coupling and phase-coherent transport in inn nanowires," *Physical Review B*, vol. 80, no. 12, p. 125321, 2009.

[34] C. Beenakker and H. van Houten, "Quantum transport in semiconductor nanostructures," *Solid state physics*, vol. 44, pp. 1–228, 1991.

[35] A. Hansen, M. Björk, C. Fasth, C. Thelander, and L. Samuelson, "Spin relaxation in inas nanowires studied by tunable weak antilocalization," *Physical Review B*, vol. 71, no. 20, p. 205328, 2005.

[36] S. E. Hernández, M. Akabori, K. Sladek, C. Volk, S. Alagha, H. Hardtdegen, M. Pala, N. Demarina, D. Grützmacher, and T. Schäpers, "Spin-orbit coupling and phase coherence in inas nanowires," *Physical Review B*, vol. 82, no. 23, p. 235303, 2010.

[37] I. Van Weperen, B. Tarasinski, D. Eeltink, V. Pribiag, S. Plissard, E. Bakkers, L. Kouwenhoven, and M. Wimmer, "Spin-orbit interaction in insb nanowires," *Physical Review B*, vol. 91, no. 20, p. 201413, 2015.

[38] N. Bouarissa and H. Aourag, "Effective masses of electrons and heavy holes in inas, insb, gasb, gaas and some of their ternary compounds," *Infrared physics & technology*, vol. 40, no. 4, pp. 343–349, 1999.

[39] G. W. Winkler, Q. Wu, M. Troyer, P. Krogstrup, and A. A. Soluyanov, "Topological phases in inas$_{1-x}$sb$_x$: From novel topological semimetal to majorana wire," *Phys. Rev. Lett.*, vol. 117, p. 076403, Aug 2016.

[40] A. Bringer and T. Schäpers, "Spin precession and modulation in ballistic cylindrical nanowires due to the rashba effect," *Physical Review B*, vol. 83, no. 11, p. 115305, 2011.

[41] R. Lassnig, "kâĘŠâŃĚ pâĘŠ theory, effective-mass approach, and spin splitting for two-dimensional electrons in gaas-gaalas heterostructures," *Physical Review B*, vol. 31, no. 12, p. 8076, 1985.

[42] R. Winkler, "Spin-orbit coupling effects in two-dimensional electron and hole systems," 2003.

[43] W. Chang, S. Albrecht, T. Jespersen, F. Kuemmeth, P. Krogstrup, J. Nygård, and C. Marcus, "Hard gap in epitaxial semiconductor–superconductor nanowires," *Nature nanotechnology*, vol. 10, no. 3, pp. 232–236, 2015.

[44] L. Yu, "Bound state in superconductors with paramagnetic impurities," *Acta Phys. Sin*, vol. 21, pp. 75–91, 1965.

[45] H. Shiba, "Classical spins in superconductors," *Progress of theoretical Physics*, vol. 40, no. 3, pp. 435–451, 1968.

[46] A. Rusinov, "Theory of gapless superconductivity in alloys with paramagnetic impurities.," tech. rep., Lebedev Inst. of Physics, Moscow, 1969.

[47] E. J. Lee, X. Jiang, M. Houzet, R. Aguado, C. M. Lieber, and S. De Franceschi, "Spin-resolved andreev levels and parity crossings in hybrid superconductor-semiconductor nanostructures," *Nature nanotechnology*, vol. 9, no. 1, pp. 79–84, 2014.

[48] W. Chang, V. Manucharyan, T. S. Jespersen, J. Nygård, and C. M. Marcus, "Tunneling spectroscopy of quasiparticle bound states in a spinful josephson junction," *Physical review letters*, vol. 110, no. 21, p. 217005, 2013.

[49] T. D. Stanescu, R. M. Lutchyn, and S. D. Sarma, "Dimensional crossover in spin-orbit-coupled semiconductor nanowires with induced superconducting pairing," *Physical Review B*, vol. 87, no. 9, p. 094518, 2013.

[50] S. D. Sarma, M. Freedman, and C. Nayak, "Majorana zero modes and topological quantum computation," *arXiv preprint arXiv:1501.02813*, 2015.

[51] L. P. Kouwenhoven, C. M. Marcus, P. L. McEuen, S. Tarucha, R. M. Westervelt, and N. S. Wingreen, "Electron transport in quantum dots," in *Mesoscopic electron transport*, pp. 105–214, Springer, 1997.

[52] A. Higginbotham, S. Albrecht, G. Kiršanskas, W. Chang, F. Kuemmeth, P. Krogstrup, T. Jespersen, J. Nygård, K. Flensberg, and C. Marcus, "Parity lifetime of bound states in a proximitized semiconductor nanowire," *Nature Physics*, vol. 11, no. 12, pp. 1017–1021, 2015.

[53] M. Deng, C. Yu, G. Huang, M. Larsson, P. Caroff, and H. Xu, "Anomalous zero-bias conductance peak in a nb–insb nanowire–nb hybrid device," *Nano letters*, vol. 12, no. 12, pp. 6414–6419, 2012.

[54] M. Deng, S. Vaitiekėnas, E. Hansen, J. Danon, M. Leijnse, K. Flensberg, J. Nygård, P. Krogstrup, and C. Marcus, "Majorana bound state in a coupled quantum-dot hybrid-nanowire system," *Science*, vol. 354, no. 6319, pp. 1557–1562, 2016.

[55] R. Meservey and P. Tedrow, "Properties of very thin aluminum films," *Journal of Applied Physics*, vol. 42, no. 1, pp. 51–53, 1971.

[56] D. Aasen, M. Hell, R. V. Mishmash, A. Higginbotham, J. Danon, M. Leijnse, T. S. Jespersen, J. A. Folk, C. M. Marcus, K. Flensberg, *et al.*, "Milestones toward majorana-based quantum computing," *arXiv preprint arXiv:1511.05153*, 2015.

[57] S. Vijay and L. Fu, "Braiding without braiding: Teleportation-based quantum information processing with majorana zero modes," *arXiv preprint arXiv:1609.00950*, 2016.